









Numerical investigation of transition on a wind turbine blade under free stream turbulence at $Re_c = 10^6$

T.C.L. Fava¹ , B.A. Lobo² , A.P. Schaffarczyk² , M. Breuer³ ,
D.S. Henningson¹  and A. Hanifi¹ 

¹FLOW, Department of Engineering Mechanics, KTH Royal Institute of Technology, SE-100 44 Stockholm, Sweden

²Mechanical Engineering Department, Kiel University of Applied Sciences, D-24149 Kiel, Germany

³Professur für Strömungsmechanik, Helmut-Schmidt-Universität Hamburg, D-22043 Hamburg, Germany

Corresponding author: T.C.L. Fava, thalesclf@gmail.com

(Received 8 December 2023; revised 20 February 2025; accepted 21 February 2025)

Laminar–turbulent transition on the suction surface of the LM45.3p blade (20 % thickness) was investigated using wall-resolved large eddy simulation (LES) at a chord Reynolds number of $Re_c = 10^6$ and angle of attack 4.6° . The effects of anisotropic free stream turbulence (FST) with intensities $TI = 0\%–7\%$ were examined, with integral length scales scaled down from atmospheric measurements. At $TI = 0\%$, a laminar separation bubble (LSB) forms and transition is initiated by Kelvin–Helmholtz vortices. At low FST levels ($0\% < TI \leq 2.4\%$), robust streak growth via the lift-up mechanism suppresses the LSB, while transition dynamics shifts from two-dimensional Tollmien–Schlichting (TS) waves ($TI = 0.6\%$) to predominantly varicose inner and outer instabilities ($TI = 1.2\%$ and 2.4%) induced by the wall-normal shear and inflectional velocity profiles. The critical disturbance kinetic energy scales with $TI^{-1.80 \pm 0.11}$, compared with $TI^{-2.40}$ from Mack’s correlation. For $TI \geq 4.5\%$, bypass transition dominates, driven by high-frequency boundary layer perturbations and streak breakdown via outer sinuous modes induced by the spanwise shear and inflectional velocity profiles. The scaling of streak amplitudes with TI becomes sub-linear and spanwise non-uniformity characterises the turbulent breakdown. The critical disturbance kinetic energy reduces to $TI^{-0.90 \pm 0.16}$, marking a transition regime distinct from modal mechanisms. The onset of bypass transition ($TI \approx 2.4\%–4.5\%$) aligns with prior studies of separated and flat-plate flows. A proposed turbulence spectrum cutoff links atmospheric measurements to wind tunnel

data and Mack's correlation, offering a framework for effective TI estimation in practical environments.

Key words: boundary layer receptivity, boundary layer stability, transition to turbulence

1. Introduction

The turbulence in the lower atmosphere is significantly affected by shear, convection, surface roughness and wakes of upstream wind turbines (Wyngaard 1992; Amandolèse & Széchényi 2004). The turbulence intensity spans $TI = 5\% - 25\%$ (Højstrup 1999; Noda & Flay 1999; Thomsen & Sørensen 1999; Hand *et al.* 2003). Despite the high TI , several works report a large region of laminar flow on the suction side of wind turbine blades (up to 40% of the chord) (Madsen *et al.* 2010; Reichstein *et al.* 2019). This is partly due to the higher relative velocity ($U_\infty = \sqrt{V_\infty^2 + (\Omega r)^2}$) felt by the blade, where V_∞ and Ωr are the wind and rotation velocities, respectively, reducing the relative TI (Schaffarczyk *et al.* 2017). The latter found $TI \approx 2\%$ and observed a laminar extent up to 20% of the chord.

The atmospheric turbulence scales help explain the protracted laminar flow. The integral length scale, representing the large eddies, may reach $\Lambda = 27 - 55$ m (IEC 2006; Bertagnolio *et al.* 2015) from wind turbine experiments. The peak in the energy spectrum occurs at $f = 0.01$ Hz, followed by a $-5/3$ -drop (Schaffarczyk *et al.* 2017). Therefore, large eddies, which are ineffective in exciting the blade boundary layer (Morkovin 1969; Saric *et al.* 2002; Schrader *et al.* 2009), carry most of the energy. Reeh (2014) interpreted the large scales (low frequencies) in the turbulence spectrum as unsteadiness in the angle of attack and pressure distribution. To compute an effective turbulence intensity (TI^{N_c}) exciting Tollmien–Schlichting (TS) waves on a blade, Madsen *et al.* (2019) used only the 100–300 Hz range of the spectrum. Schaffarczyk *et al.* (2017) highlighted the need for such a cutoff, but its selection criterion is unclear. This consists in selecting the low-frequency cutoff $N_c > 0$ in

$$TI^{N_c} = \sqrt{\frac{(u'_{rms})^2 + (v'_{rms})^2 + (w'_{rms})^2}{3}} \stackrel{N_c=0}{=} TI, \quad (1.1)$$

$$u'_{rms} = \sqrt{\frac{1}{N^2} \sum_{N_c} |\hat{u}|^2 \stackrel{N_c=0}{=} \sqrt{\frac{1}{N} \sum_0^N u'^2} = u'_{rms}, \quad (1.2)$$

where $u' = U - \bar{U}$ (similarly for v'_{rms} and w'_{rms}), with U and \bar{U} representing the instantaneous and mean x velocity, \hat{u} the single-sided frequency spectrum of u' , and N the time-series length; r.m.s. stands for root mean square. The comparison between wind tunnel and atmospheric turbulence from flight data suggests this threshold may be at $f \approx 300$ Hz, removing the inertial sub-range from the latter (Romblad *et al.* 2022). Obtaining an effective TI from wind turbine data is particularly interesting for usage with Mack's empirical relation (Mack 1977) between the critical N factor (N_{tr}) and TI given by

$$N_{tr} = -8.43 - 2.40 \cdot \ln(TI/100). \quad (1.3)$$

Mack's correlation is obtained from wind tunnel data of a flat plate under zero pressure gradient and grid turbulence. Here, N_{tr} is used for transition estimation with the e^N method (Smith & Gamberoni 1956; van Ingen 1956). Transition occurs for $\ln[A/A(x_0)] =$

N_{tr} , where A is the disturbance amplitude and x_0 is the location of initial growth. This method has been successful for natural or TS-dominated transition (Arnal & Casalis 2000; van Ingen 2008), but bypass transition for $TI \gtrsim 0.5\% - 1\%$ (Morkovin 1969; Reshotko 1976; Arnal & Juillen 1978; Boiko *et al.* 2002) and flow separation (Fava *et al.* 2023c) limit its use.

The transition scenario depends on the receptivity process. Linear receptivity may occur for $TI < 3\%$ (Brandt *et al.* 2004), where small vortices diffuse into the boundary layer (Bertolotti 1997). Shear sheltering prevents high-frequency perturbations from entering the boundary layer (Hunt & Carruthers 1990; Jacobs & Durbin 1998). Nonlinear receptivity due to the interaction of oblique waves in the free stream turbulence (FST) is the primary excitation source for higher TI (Berlin *et al.* 1999). Blanco *et al.* (2024) separated the linear and nonlinear receptivity effects in the Blasius boundary layer, showing that the former generates streaks with energy $E \propto TI^2$ near the leading edge and the latter creates streaks with $E \propto TI^4$ further downstream. Faúndez Alarcón *et al.* (2022) and Fava *et al.* (2023c) studied aerofoil receptivity to FST injected outside the boundary layer, showing that optimal perturbation analysis explained the initial disturbance growth for low TI . Large-scale disturbances can also excite shorter wavelength perturbations through scale conversion/reduction, enabled by fast base-flow variations near the leading edge (Goldstein 1983; Ruban 1984).

A boundary layer may have a modal instability regime for low TI characterised by disturbance growth dominated by the eigenmodes (e.g. TS and Kelvin–Helmholtz (KH) modes) of the linearised Navier–Stokes operators (Reed *et al.* 1996). The non-modal scenario (Schmid 2007) is associated with the transient growth of vortical perturbations (Butler & Farrell 1992), which may lead to streamwise elongated structures denominated streaks (Klebanoff 1971). The latter grow via the lift-up mechanism (Landahl 1975, 1980), whose optimal initial disturbances are streamwise vortices (Andersson *et al.* 1999; Luchini 2000). The streaks may trigger an inner mode, i.e. the secondary instability of TS waves, with a near-wall critical layer (Vaughan & Zaki 2011). It develops a checkered pattern over the streaks with lambda structures at the intersection of high- and low-speed streaks (Nagarajan *et al.* 2007; Schlatter *et al.* 2010; Vaughan & Zaki 2011) or hairpin vortices on the sides of the streak (Hack & Zaki 2014). This mode relies on the excitation near the leading edge (Schrader *et al.* 2010). The increase in the adverse pressure gradient (APG) enhances the amplification of the inner mode and turbulent breakdown (Hack & Zaki 2014), whereas increasing amplitude and decreasing frequency of streaks have the opposite effect (Vaughan & Zaki 2011). The latter found a maximum phase speed $c_p = 0.54U_\infty$ for the inner modes.

The outer mode is linked to the secondary instability of the streaks, with a critical layer far from the wall. Its dominance occurs for higher TI and is associated with bypass transition, being a precursor of turbulent spots (Asai *et al.* 2002; Mans *et al.* 2005, 2007). It can manifest as spanwise symmetric and antisymmetric oscillations around the streak centreline denominated varicose and sinuous instabilities (Swearingen & Blackwelder 1987). The increase in the APG favours a change from the sinuous to the varicose types (Marquillie *et al.* 2011). The sinuous instability may be more unstable (Andersson *et al.* 2001), triggered for a minimum amplitude of $0.085U_\infty$ (Arnal & Juillen 1978; Mandal *et al.* 2010; Vaughan & Zaki 2011). Varicose and sinuous outer modes are related to inflectional velocity profiles in the wall-normal and spanwise directions, respectively (Brandt *et al.* 2004). The varicose mode may occur by colliding aligned high- and low-speed streaks, forming a lambda vortex, which was confirmed experimentally by Balamurugan & Mandal (2017). This leads to a spatially discontinuous shear layer that allows high-frequency FST disturbances to infiltrate the boundary layer, leading to hairpin

vortices and turbulent spots (Brinkerhoff & Yaras 2015). The sinuous instability may arise by a misaligned collision of high- and low-speed streaks (Brandt & de Lange 2008) and frequently occurs in the rear part of the former (Mans *et al.* 2007). Vaughan & Zaki (2011) found a maximum phase speed of $0.75U_\infty$ for the outer modes. For high TI , inner and outer instabilities may be suppressed, and the turbulent breakdowns may be directly caused by the FST forcing (Zhao & Sandberg 2020).

Hosseini-verdi & Fasel (2019) showed that an exponential amplification follows the initial slow algebraic growth of streaks in the APG region of a flow with separation. These authors identified transition dominated by KH modes for $TI = 0.1\%$, streaks for $TI = 2\% - 3\%$, and both for intermediate TI . Istvan & Yarusevych (2018) demonstrated that streaks contribute more to the disturbance kinetic energy than KH modes for an aerofoil with flow separation for $TI > 1.99\%$. They noted that high TI leads to decreased spatial amplification, suggesting that the increased initial disturbance amplitudes in this regime primarily cause earlier transition. Jaroslawski *et al.* (2023) indicated that an increase in TI attenuates the growth of modal instabilities, and the streamwise energy growth shifts from exponential to algebraic for high disturbance levels. Dotto *et al.* (2022) noted that discrete and continuous Orr–Sommerfeld modes were relevant for transition for a zero APG boundary layer for $TI = 2\% - 3\%$.

Transition on wind turbine blades was investigated with surface microphones (Özçakmak *et al.* 2020). Natural transition was observed in wind-tunnel (Madsen *et al.* 2010; Lobo *et al.* 2018) and field (Trolborg *et al.* 2013) experiments for low TI , characterised by a pronounced amplitude peak in the microphone pressure spectrum. Bypass transition occurred when the blade passed through the wake of upstream wind turbines, with the microphone pressure spectrum presenting high energy for low frequencies ($f < 10$ Hz) and no clear peak (Özçakmak *et al.* 2020; Lobo *et al.* 2023). Dollinger *et al.* (2019) and Reichstein *et al.* (2019) detected wedges aligned with azimuthal direction signalling bypass transition. There are other experimental works on the role of FST on wind turbines, but they do not provide further insight into transition (Døssing 2008; Bertagnolio *et al.* 2015; Schaffarczyk *et al.* 2017; Madsen *et al.* 2019; Reichstein *et al.* 2019; Oehme *et al.* 2022). Wind-tunnel investigations with grid turbulence and integral length scale $O(10^{-1})$ m showed an enhancement in the blade performance due to bypass transition and suppression of flow separation (Amandolèse & Széchényi 2004; Sicot *et al.* 2008; Maldonado *et al.* 2015).

The literature on how FST affects transition is dense, but there is limited understanding of how it occurs on wind turbine blades. Pertinent issues include: (i) the assessment of Mack’s correlation; (ii) a cutoff for the size of free stream eddies affecting transition; (iii) a TI threshold for bypass transition; (iv) a better understanding of receptivity, and the stabilising or destabilising interaction between streaks and modal instabilities. This work attempts to address these questions with detailed wall-resolved large eddy simulation (LES) of a wind turbine aerofoil at a Reynolds number $Re_c = 10^6$ under FST intensities $TI = 0\%, 0.6\%, 1.2\%, 2.4\%, 4.5\%$ and 7% . This study extends the results of Lobo *et al.* (2022) and Fava *et al.* (2023c) to a realistic Re_c of wind turbines. The manuscript is divided as follows: § 2 presents the numerical set-up and test cases; § 3 contains the results and is subdivided into several subsections; § 3.1 characterises mean and instantaneous fields; § 3.2 investigates the receptivity process; § 3.3 analyses the evolution of modal and non-modal disturbances, and applies linear stability theory; § 3.4 proposes a low-frequency cutoff for FST; and finally, § 4 presents the conclusions. Appendix A summarises the calculations of coefficients and errors of linear regression of the critical N factor correlations. Appendix B shows the operators for stability analysis

	Velocity component		
	Longitudinal	Lateral	Vertical
Standard deviation σ_k	σ_1	$0.8 \sigma_1$	$0.5 \sigma_1$
Integral scale, Λ_k	$8.1 \Lambda_1$	$2.7 \Lambda_1$	$0.66 \Lambda_1$

Table 1. Kaimal length scales and standard deviation ratios from IEC 61400-1 (IEC 2006).

on cross-planes. Appendix C displays the statistics of the time variation of the pressure coefficient due to the FST.

2. Study cases and numerical approach

2.1. Description of flow cases

The flow on the suction side of a 20 % thick aerofoil, employed at a radius of 35 m of the LM45.3p blade of the 2 MW Senvion MM92 wind turbine, is analysed for an angle of attack $AoA = 4.6^\circ$. The Reynolds number based on the free stream velocity (U_∞) and chord length (c) is $Re_c = 10^6$. Unless otherwise stated, the dimensional variables (denoted by *) are non-dimensionalised by U_∞ and c . FST intensities $TI = 0\%$, 0.6% , 1.2% , 2.4% , 4.5% and 7% are considered.

Two coordinate systems are employed. The x , y , z coordinates are in the chord direction ($x = 0$ at the leading edge and $x = 1$ at the trailing edge), wall-normal direction (y) and spanwise direction (z). The U , V and W velocities are in the streamwise (along the aerofoil), wall-normal (y) and spanwise (z) directions. The second coordinate system, \bar{x} , \bar{y} , \bar{z} , is only used for the generation of FST. Note that \bar{x} is aligned with the inflow direction and forms an $AoA = 4.6^\circ$ with x , whereas \bar{z} is aligned with z . Specifically for the generation of FST, U , V and W are in the \bar{x} , \bar{y} and \bar{z} directions. The anisotropic FST is based on the IEC-61400-1 standard (IEC 2006), with integral length scales (Λ_k) and standard deviation (σ_k) ratios given in table 1. They follow a Kaimal spectrum (Kaimal 1973) represented by (2.1), where \bar{U} is the hub-height mean velocity:

$$E(f) = \sigma_k^2 \frac{4\Lambda_k/\bar{U}}{(1 + 6f\Lambda_k/\bar{U})^{\frac{5}{3}}}. \quad (2.1)$$

Here, $\Lambda_1 = 42$ m for hub heights greater than 60 m (IEC 2006). A wall-resolved LES of such large scales is computationally expensive. Therefore, the structures are scaled down, keeping the ratio between the length scales in the three directions, so that they fit within the spanwise width $L_z = L_z^*/c = 0.06$ (the limiting domain dimension). The maximum energy is located in the spanwise wavenumber $k_z = \sqrt{\pi}/L_z$, where k_z is a variable. The maximum spanwise wavelength that can be resolved is based on the spanwise dimension such that $\lambda_z = 2\pi/k_z = 0.06$. The two-point correlations along the span of the spanwise velocity drop to zero in the range $l_{corr} = 0.012-0.019$ considering all studied cases. The fact that $l_{corr} < 0.03 = L_z/2$ ensures that the domain is not forcing an artificial spanwise periodicity.

Together with the relations from table 1, it is found that the length scales in the \bar{x} , \bar{y} and \bar{z} directions are 0.211, 0.07 and 0.01 dimensionless units, respectively.

2.2. Details of the numerical method

The Navier–Stokes equations for an incompressible flow are solved using a classical wall-resolved LES methodology with the code *LESOC* (Breuer 1998, 2000, 2018;

Breuer & Schmidt 2019). It employs a finite-volume method on a curvilinear and block-structured grid. The solver is second-order accurate in space and time. The dynamic variant (Germano *et al.* 1991; Lilly 1992) of the classical Smagorinsky subgrid-scale model (Smagorinsky 1963) is applied, as Sayadi & Moin (2011) showed the former has several advantages necessary for predicting transitional flows. FST is generated with the digital filter method of Klein *et al.* (2003), improved for numerical efficiency by Kempf *et al.* (2012). The method relies on discrete linear digital non-recursive filters and requires only a few statistical properties for generating FST with proper auto-correlations in time and two-point correlations in space. Realistic cross-correlations between the three velocity components are achieved with the transformation by Lund *et al.* (1998).

The inflow turbulence generator inputs are the mean velocity, Reynolds stresses, and integral time (T) and length scales ($\Lambda_{\bar{x}}$, $\Lambda_{\bar{y}}$, $\Lambda_{\bar{z}}$). Here, T can be obtained from $\Lambda_{\bar{x}}$ using Taylor's frozen turbulence hypothesis. The three normal components of the Reynolds stresses are calculated by first determining the turbulent kinetic energy (TKE or k) considering isotropic turbulence as $k = (3/2)TI^2$. Next, using the relations between the standard deviations in table 1 and the equation for the turbulent kinetic energy $k = (1/2)(\overline{u'_x u'_x} + \overline{u'_y u'_y} + \overline{u'_z u'_z})$, the three normal components of the Reynolds stress tensor for anisotropic FST are determined. To allow for a streamwise–spanwise correlation, a non-zero Reynolds shear stress is included. This can be set as $\overline{u'_x u'_z} = -U_{star}^2$, where $U_{star} = 0.05$ is the friction or shear velocity, which depends on the ground roughness scale (Jonkman 2009). Here, $U_{star} = 0.05$ is arbitrarily selected. The direction of the non-zero Reynolds shear stress is chosen to be $\overline{u'_x u'_z}$ since the spanwise direction (z) is the component in the direction from the blade root to the tip and the effect of shear within the rotor plane, mainly due to the ground, is important to consider. Other turbulence generators in the wind industry, such as TurbSim (Jonkman 2009), also consider this component for computing U_{star} .

The inflow generator only allows one length scale per direction. This drawback is overcome by the superposition of inflow turbulence with different length scales, given by the maximal length scale divided by a factor $2^{(n-1)}$, where n is the index of the superimposed signal. The smallest scales that can be resolved depend on the computational grid. Here, $n = 6$ is retained. To respect Kolmogorov's $k^{-5/3}$ law, the following steps are employed in the scaling.

- (i) The frequency of each subsequent velocity signal is scaled by a factor of $2^{(n-1)}$.
- (ii) Next, since $k \propto u_i'^2$, the velocity fluctuations are scaled by a factor of $2^{1/2}$ to represent their contribution to the TKE. This leads to an intermediate scaling factor of $2^{(n-1) \times (1/2)}$.
- (iii) Finally, k should decay according to Kolmogorov's $k^{-5/3}$ law and thus, the velocity fluctuations must further be scaled by $2^{-5/3}$ leading to the final scaling factor to be used, that is, $2^{(n-1) \times (-5/3 \times 1/2)} = 2^{(-5/6) \times (n-1)}$.

The resulting fluctuating velocity signal $u_{\bar{x},sum}$ (similarly for $u_{\bar{y},sum}$ and $u_{\bar{z},sum}$) is obtained by weighing the original signals by this scaling factor for each n and superimposing them. For obtaining the required TI and TKE spectrum, $u_{\bar{x},sum}$ is normalised according to

$$u_{\bar{x},sum} \leftarrow u_{\bar{x},sum} / \sqrt{sum_w}, \quad sum_w = \sum_n \left[2^{\frac{-5}{6}(n-1)} \right]^2, \quad (2.2)$$

where sum_w is the total contribution of the weights to the TKE.

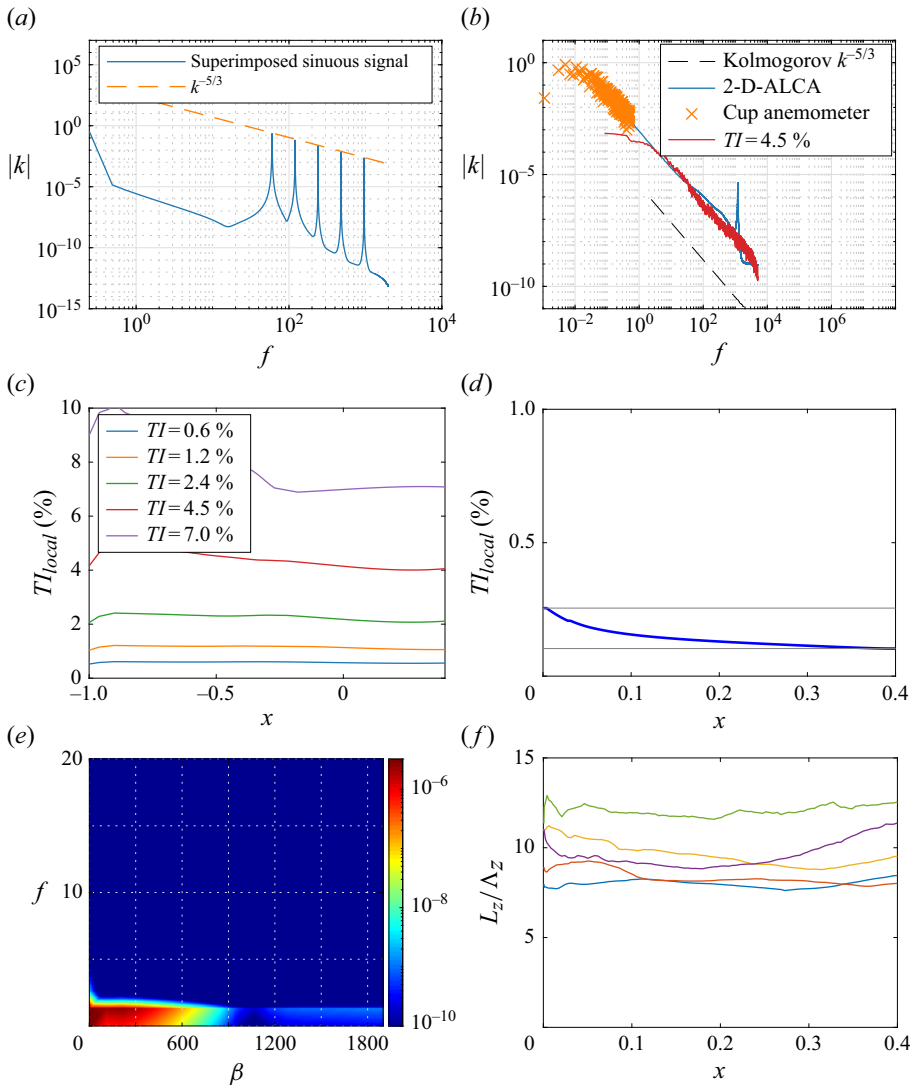


Figure 1. Turbulent kinetic energy spectra of the (a) superimposed sinusoidal signals, (b) synthetic inflow turbulence compared with atmospheric measurements from Jeromin *et al.* (2014). (c) Variation of the turbulence intensity at $y = 120\delta^*$ as a function of x . (d) Local turbulence intensity at $y = 120\delta^*$ as a function of x for $TI = 0\%$. (e) Spectrum of perturbation kinetic energy at $y = 120\delta^*$ at the leading edge for $TI = 0\%$. (f) Ratio of the domain spanwise width to the spanwise integral length scale of the synthetic inflow turbulence with $x = 0$ corresponding to the leading-edge of the aerofoil.

For simplicity, the scaling is illustrated with the help of six sinusoidal signals with frequencies $2^{(n-1)}f$, where $f = 60$ and $n = 1-6$. Figure 1(a) portrays the turbulent kinetic energy spectrum with the scaling as described in the procedure above, where the resulting signal follows Kolmogorov's $k^{-5/3}$ law.

The inflow turbulence is injected inside the domain, one chord length upstream of the aerofoil ($x = -1$), in a region with a streamwise length $2\Lambda_{\bar{x}}$. A special source-term formulation, developed and validated in several studies (Schmidt & Breuer 2017; Breuer 2018; De Nayer *et al.* 2018; Breuer & Schmidt 2019), is employed for that. A comparison of the turbulent kinetic energy spectrum of the generated FST with measurements from the

free atmosphere is shown in [figure 1\(b\)](#). The measurements are from a two-dimensional (2-D) atmospheric laser cantilever anemometer (ALCA, blue line) and cup anemometers (red symbols) in the lower atmosphere (Jeromin *et al.* 2014). The power spectral density is normalised by $\int_0^\infty S(f) \cdot df = (1/2)\langle \|\mathbf{u}'\|^2 \rangle$. The synthetic turbulence agrees with the measured data above a minimum frequency. [Figure 1\(c\)](#) indicates that the turbulence intensity decays from the injection point to $x = -0.4$, downstream of which its decrease is not significant, approximately reaching the nominal values of $TI = 0.6\%$, 1.2% , 2.4% , 4.5% and 7% affecting the aerofoil ($x = 0-1$). [Figure 1\(d\)](#) quantifies the background noise levels for $TI = 0\%$, showing that the local turbulence level spans 0.1% – 0.25% from the aerofoil leading edge to 40% of the chord. [Figure 1\(e\)](#) shows the perturbation kinetic energy spectrum at $y = 120\delta^*$ at the leading edge, which indicates that the disturbances display mainly low frequency ($f < 2$) and spanwise wavenumber (β), with a predominance of 2-D perturbations.

2.3. Computational domain and grid resolution

The C-type grid included the angle of attack of 4.6° and extended 8 and 15 chord lengths upstream and downstream of the aerofoil, respectively. The spanwise width $L_z = 0.06$ was selected such that $L_z/\Lambda_z > 8$, as shown in [figure 1\(f\)](#), respecting the minimum $L_z/\Lambda_z = 6$ proposed by O'Neill *et al.* (2004) and followed by Faúndez Alarcón *et al.* (2022). Although respecting these guidelines from the literature, the limited spanwise width is expected to have some influence on the flow structures. A wider domain enables a higher decorrelation of the structures in the spanwise direction. Conversely, a relatively narrow domain with spanwise periodic boundary conditions may artificially increase the spanwise correlation of the turbulence structures, reducing their spatial heterogeneity. The narrow domain may also constrain global modes arising in laminar separation bubbles (LSBs) to have an artificially high spanwise wavenumber since these modes may typically present large spanwise wavelengths, comparable to those of the length of the LSB (Fava *et al.* 2024b). As will be discussed in § 3, the only case with separation is $TI = 0\%$, but the reverse flow is too low to allow a global mode. Finally, the narrow domain limits the number of streaks that can fit the domain side by side, which may preclude or underpredict instabilities related to lateral interactions between streaks.

The time step is $\Delta t^* \cdot U_\infty/c = 3 \times 10^{-6}$, yielding a maximum Courant number of 0.26. The total run time was $25 U_\infty/c$, with statistics collected for the last $8 U_\infty/c$, sufficient for the temporal convergence of the Reynolds stresses.

A wall-orthogonal grid was generated with $y_{1st}^+ < 1.0$ (first cell centre) and expansion factor of 1.05, $\Delta x^+ \leq 30$ (suction side), $\Delta x^+ \leq 60$ (pressure side) and $\Delta z^+ \leq 25$. This mesh resolution respects the criteria for wall-resolved LES outlined by Piomelli & Chasnov (1996). On the suction side, the mesh respects the more restrictive criteria proposed by Asada & Kawai (2018) for transitional flows with separation and streaks. The dimensionless grid parameters are similar to those in earlier studies at $Re_c = 1 \times 10^5$ (Lobo *et al.* 2022; Fava *et al.* 2023c). A grid-independence study was conducted with a finer grid with nearly three times the number of points of the standard grid and is available from Lobo (2023).

3. Results

3.1. General flow analysis

[Figure 2](#) exhibits the spanwise- and time-averaged streamwise velocity ($\langle U \rangle_{z,t}$) profiles at $x = 0, 0.1, \dots, 1$. The edge of the mean LSB, defined as $(x, y) \in \int_0^y \langle U \rangle_{z,t}(x, \xi) d\xi = 0$,

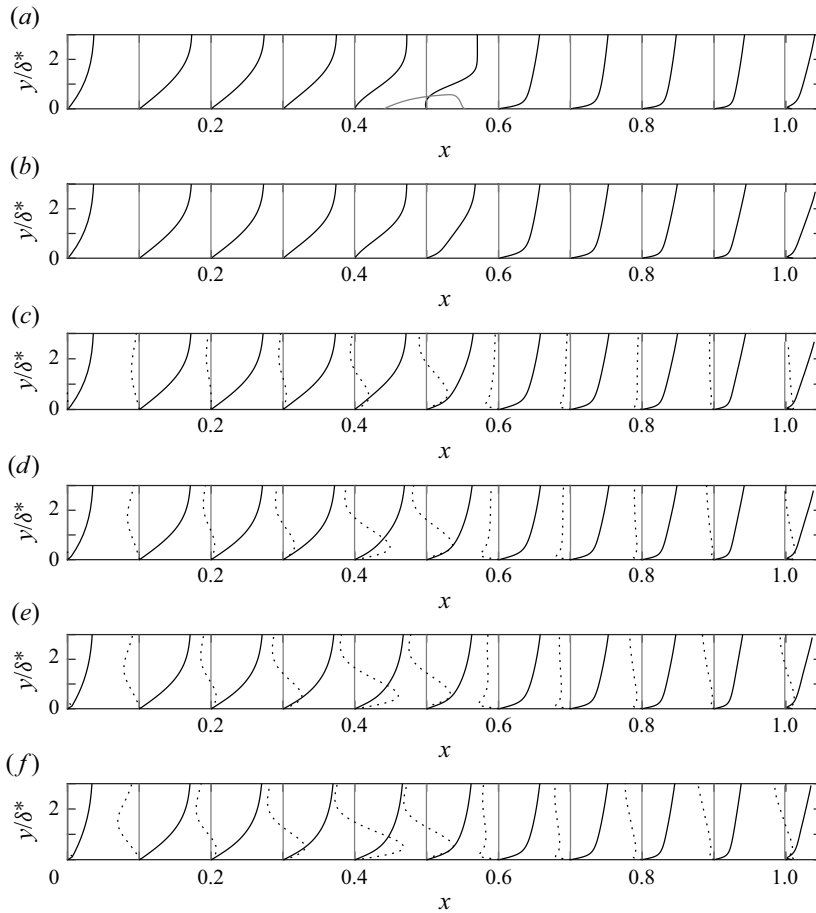


Figure 2. Wall-normal profiles of spanwise- and time-averaged streamwise velocity (—) and mean streamwise velocity distortion (MFD,) for (a) $TI = 0\%$, (b) 0.6% , (c) 1.2% , (d) 2.4% , (e) 4.5% and (f) 7% . The LSB edge (normalised by δ^*) is denoted by —. The MFD is magnified four times for enhanced visibility.

is shown for $TI = 0\%$ in [figure 2\(a\)](#). The LSB lies in the $x = 0.44\text{--}0.55$ region, with a maximum height $h_{max}/\delta^* = 0.57$ at $x = 0.53$ and reverse flow of -7% of U_∞ . The APG acting downstream of $x = 0.26$ is the main driver of flow separation. The transition location (x_{tr}) is defined as the streamwise locus of maximum $\langle u'_{rms} \rangle_z$. For $TI = 0\%$, $x_{tr} = 0.55$ indicates that flow reattachment occurs nearly immediately after transition. Low levels of FST, such as $TI = 0.6\%$ in [figure 2\(b\)](#), are enough to suppress separation unlike found in previous studies at $Re_c = 10^5$ (Lobo *et al.* 2022; Fava *et al.* 2023c). The spanwise-averaged part of the mean flow distortion (MFD), i.e. $\langle U \rangle_{z,t} - \langle U \rangle_{z,tI=0.6\%}$, is also presented for $TI > 0.6\%$. Although the separation suppression is an effect of the MFD (Marxen & Rist 2010), $TI = 0.6\%$ is selected as the base case instead of $TI = 0\%$ to isolate the effect of non-modal growth on the mean profiles. The MFD becomes positive near the wall as streamwise momentum is transferred to this region by the lift-up mechanism. Moreover, the MFD increases in the streamwise direction as the streaks grow, reaching a maximum at $x = 0.4$ or 0.45 . This maximum increases monotonically with TI . After transition, the MFD quickly becomes negative as turbulent mixing diffuses momentum across the wall-normal direction.

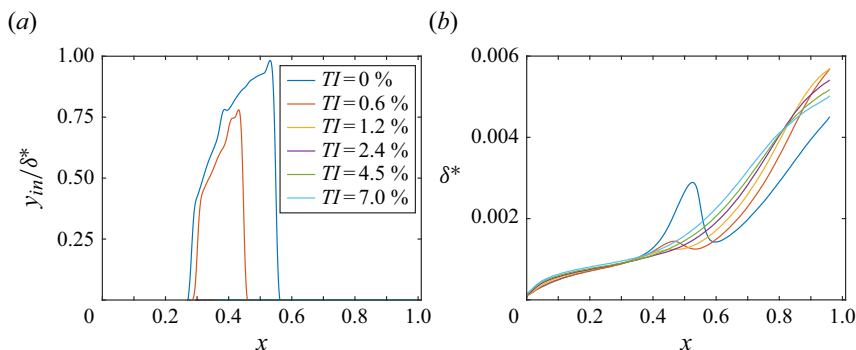


Figure 3. (a) Wall-normal location of the inflection point in the spanwise- and time-averaged streamwise velocity profiles. (b) Displacement thickness (δ^*).

The capacity of the flow sustaining inflectional instabilities is assessed with the wall-normal location of the inflection point in $\langle U \rangle_{z,t}$ (y_{in}) in figure 3(a), non-dimensionalised by the displacement thickness (δ^*). The mean flow is inflectional for $TI \leq 0.6\%$, indicating susceptibility to inflectional instabilities. The farther the inflection point from the wall, the stronger is this type of mechanism. Thus, the flow is more unstable for $TI = 0\%$, where the peak value $y_{in}/\delta^* \approx 1$ agrees with Veerasamy *et al.* (2021) and Jaroslowski *et al.* (2023), and occurs at the LSB maximum height location ($x_{h_{max}} = 0.53$). The relatively high values of y_{in}/δ^* for $TI = 0.6\%$ also indicate a potential role of an inflectional instability. For $TI \geq 1.2\%$, the mean flow is not inflectional, hence not susceptible to inflectional instability. The evolution of δ^* is shown in figure 3(b). The local maximum in δ^* in the mid-chord region is due to the near-wall mass flux deficit, which promotes an increase in δ^* , followed by transition to turbulence, which locally reduces δ^* via turbulent mixing. The case with flow separation ($TI = 0\%$) has the highest mass flux deficit and, therefore, the most pronounced increase in δ^* . Even though the $TI = 0.6\%$ case does not present flow separation, it displays a reduced mass flux deficit due to the APG in the laminar flow region. This leads to a local increase in δ^* , similar to, but less pronounced than, $TI = 0\%$. The increase in TI reduces the near-wall mass flux deficit, since turbulent mixing brings high-momentum fluid to this region, and the local maximum in δ^* is progressively attenuated.

Figure 4 shows the streamwise velocity fluctuations (u') on a wall-parallel plane corresponding to a height of δ^* at 20% chord and for arbitrary time. For $TI = 0\%$ in figure 4(a), 2-D rolls emerge at $x = 0.44$, which as seen from figure 2(a) lie in the LSB. The separation (S) and reattachment (R) lines are indicated. The rolls are characteristic of a KH instability of the separated shear layer (Jaroslowski *et al.* 2023), as confirmed later in the analyses.

For $TI = 0.6\%$, the isolines of Q -criterion ($Q = 250$) are superimposed on the contours of u' in figure 4(b), indicating spanwise rolls at $x = 0.46$ – 0.5 . However, these are not KH modes since neither instantaneous nor mean flow separation is detected (see figure 2b). Moreover, they occur downstream of the mean inflectional flow region ($x = 0.27$ – 0.46), depicted in figure 3(a). Figure 5(a) shows the wall-normal $|u'|$ profile at $x = 0.54$, $z = 0.02$, where these rolls occur, for the same instant as figure 4(b). The profile corresponds to the standard TS waves from Schlatter *et al.* (2010). However, at $z = 0.06$, where a streak passes, the profile presents a local maximum around $y/\delta^* = 2$, in agreement with the streaky TS waves computed by Schlatter *et al.* (2010). Cossu & Brandt (2004) attributed these modes to the fundamental secondary instability of the TS waves in the streaky

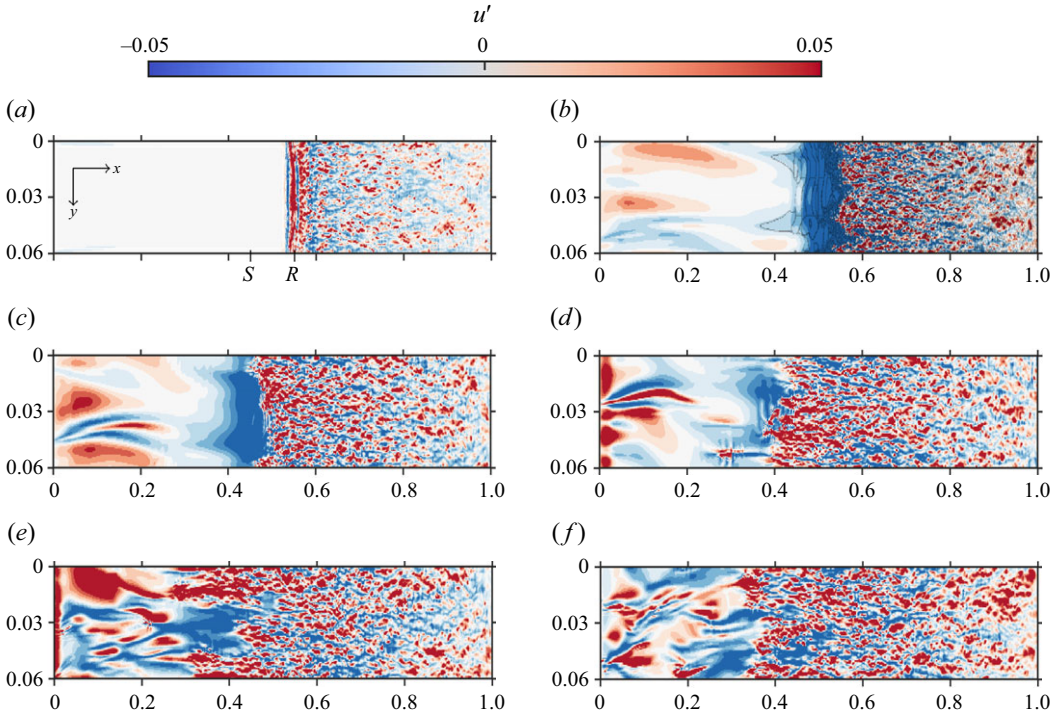


Figure 4. Streamwise velocity fluctuations ($u' = U - \langle U \rangle_{z,t}$) on a wall-parallel plane at a height of δ^* for (a) $TI = 0\%$, (b) 0.6% , (c) 1.2% , (d) 2.4% , (e) 4.5% and (f) 7% . Here S and R denote flow separation and reattachment. The isolines of Q -criterion ($Q = 250$) are also shown for $TI = 0.6\%$.

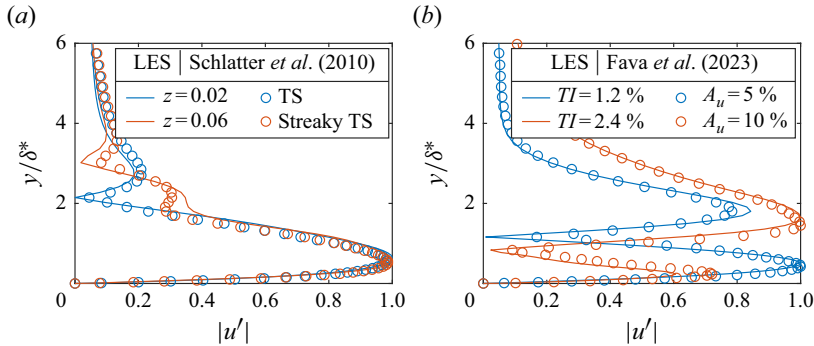


Figure 5. Wall-normal profiles of the absolute value of the instantaneous streamwise velocity fluctuations for (a) $TI = 0.6\%$ at $x = 0.5$ and (b) $TI = 1.2\%$ and 2.4% at $x = 0.4$, $z = 0.02$ considering the same time as figure 4. In panel (a), the results are compared with the profiles of TS and streaky TS waves from Schlatter *et al.* (2010) (circles). In panel (b), the results are compared with the profiles of inner modes from Fava *et al.* (2023b) (circles) for base streaks with amplitudes of $A_u = 5\% U_\infty$ and $10\% U_\infty$.

flow. Therefore, the streaky TS waves correspond to the inner modes of Vaughan & Zaki (2011).

The time–space evolution of the streak observed at $x = 0.2$, $z = 0.01$ for $TI = 0.6\%$ in figure 4(b) is investigated. The convection speed of the streak is $0.67 u_e \approx 1$, where u_e is the boundary layer edge velocity. Figure 6 shows contour plots of the streamwise velocity

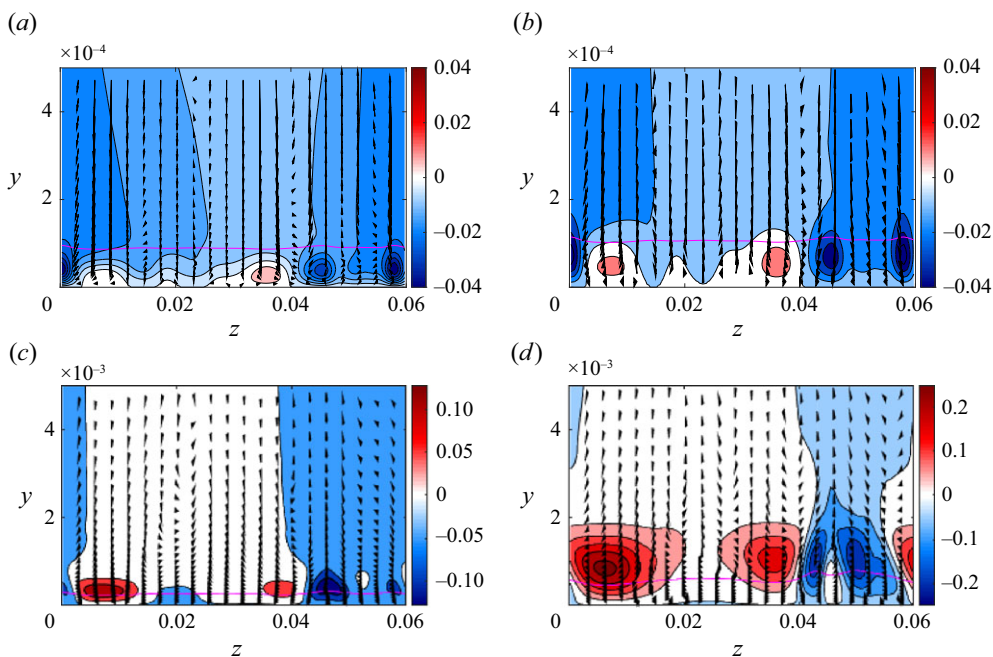


Figure 6. Contours of streamwise velocity fluctuations on a cross-sectional plane at (a) $x = 0.001$, (b) $x = 0.002$, (c) $x = 0.038$, (d) $x = 0.2$ for $TI = 0.6\%$ following the same streak as in figure 4(b). The vectors of fluctuating velocities on this plane are also shown (not to scale). The magenta line indicates δ^* .

fluctuations (u') on the cross-sectional planes from the leading edge to $x = 0.2$. The vectors of fluctuating velocities on this plane, i.e. (w' , v'), are also shown (not to scale). The streak is generated near the leading edge ($x = 0.001$, panel a), where there is an influx of high-momentum fluid from the top of the boundary layer to the near-wall region, generating high-speed fluctuations in this area for $z = 0 - 0.04$. For $z = 0.04 - 0.06$, the low-speed fluid near the wall is lifted, generating a low-speed distortion. This is typical of the lift-up mechanism responsible for the amplification of the streaks. Furthermore, the diffusion of free stream vortices into the boundary layer is characteristic of linear receptivity (Bertolotti 1997). Note that δ^* is nearly constant along z and only undergoes small modifications further downstream, implying these structures are not due to a temporary thinning (or thickening) of the boundary layer. The streaks quickly grow at $x = 0.002$ (panel b) and $x = 0.038$ (panel c), rising above δ^* in the latter location. Finally, at $x = 0.2$ (panel d), the streaks are fully formed with a spanwise scale within the range of those observed by Brandt *et al.* (2004), for example, which is $l_{streaks} = (4-7)\delta^*$. Moreover, the streamwise vortices characteristic of the lift-up mechanism are present in the vector field.

The number and amplitude of streaks increase for $TI = 1.2\%$, as shown in figure 4(c). However, the transition line is spanwise uniform without early turbulent spots. The wall-normal $|u'|$ profile in figure 5(b) agrees with the inner modes computed by Fava *et al.* (2023b) with linear stability analysis for base streaks with an amplitude $A_u = 5\% U_\infty$. The $TI = 2.4\%$ case in figure 4(d) presents isolated instabilities over individual streaks (e.g. at $x = 0.3$, $z = 0.04 - 0.06$). The disturbance profile in figure 5(b) agrees with that from Fava *et al.* (2023b) for base streaks with $A_u = 10\% U_\infty$. The outer maximum increases in magnitude compared with the near-wall maximum, suggesting an increased importance of outer modes. However, the near-wall maximum is still 75% of the outer maximum, which shows that inner modes play a significant role in this case. This agrees with

Bose & Durbin (2016), who found inner modes essential for transition at $TI \approx 2\%$. The non-uniformity becomes much more pronounced for $TI = 4.5\%$ and 7% in figures 4(e) and 4(f), where individual streak breakdowns are the rule, indicating the dominance of the outer modes and bypass transition. Streaky TS waves are not observed. This agrees with Hosseinverdi & Fasel (2019), who found the transition dominated by streaks for $TI > 3\%$. Indeed, the increase in the streak amplitude mitigates the inner modes while enhancing the outer ones (Vaughan & Zaki 2011).

3.2. Receptivity

The boundary-layer receptivity to FST is analysed. The spectra of perturbation kinetic energy ($|k'|$) at the leading edge, where receptivity mainly occurs, are shown in figure 7. The left and centre columns portray the $|k'|$ -spectra at $y = 120\delta^*$ and $y = \delta^*$, respectively. The right column presents the ratio between $|k'|$ at $y = \delta^*$ and $y = 120\delta^*$. For $TI = 0\%$, the disturbance amplitude outside the boundary layer is very low (panel a). There is an amplification of three-dimensional disturbances centred around $f = 2.7$ and $\beta = 1057.3$ ($n_z = L_z\beta/(2\pi) = 10$) as shown in panel (c), but the disturbance amplitude remains low inside the boundary layer (panel b). This phenomenon may be due to non-modal growth (Schmid 2007) since the mean flow in this region will later be shown to be modally stable (in the local sense) but prone to transient growth. For $TI = 0.6\%$ (panels d,e,f) and $TI = 1.2\%$ (panels g,h,i), the maximum amplitudes outside and inside the boundary layer occur at low- f , low- β . However, high- f , high- β disturbances are mainly excited, as seen in panel (f,i). However, the perturbation amplitudes inside the boundary layer in this zone of the spectrum remain low. This changes for $TI = 2.4\%$ (panels j,k,l), $TI = 4.5\%$ (panels m,n,o) and $TI = 7\%$ (panels p,q,r) for which the regions of high gain overlap with areas of high disturbance amplitude ($O(10^{-5})$ in the centre column). The excitation of high-frequency vortical disturbances inside the boundary layer is associated with bypass transition (Zaki & Durbin 2005). These disturbances are most likely excited by nonlinear interactions (Berlin *et al.* 1999; Schrader *et al.* 2009) since shear sheltering attenuates the penetration of high-frequency disturbances into the boundary layer (Durbin 2017).

Figure 8(a,b,c) shows the streamwise evolution of $|u'|$ for three of the highest-amplitude (f, β) fluctuations in the flow. These disturbances have low frequency and they are induced in the boundary layer by the FST, especially near the leading edge, where they grow more rapidly. The lower amplitude of high-frequency fluctuations is possibly related to shear sheltering. The scaling of $|u'|$ with TI is assessed in figure 8(d,e,f), where there is good agreement between the scaled curves for $TI \leq 2.4\%$ for $f = 2.7, \beta = 104.7$ and $f = 2.7, \beta = 209.4$ (centre and right columns). The scaling is not as good for $f = 1.3, \beta = 104.7$, but the curves are clustered for $TI \leq 1.2\%$ and $TI \geq 4.5\%$, separately. These results suggest that linear receptivity occurs for $TI \leq 1.2\%$ and possibly also for $TI = 2.4\%$. Brandt *et al.* (2004) found that linear receptivity occurred at $TI < 3\%$ in Blasius flow, which supports the current results. Figure 8(g,h,i) shows that the curves do not scale well with TI^2 , suggesting that nonlinear receptivity is not dominant in the generation of the leading boundary-layer perturbations. However, lower amplitude disturbances with high f and β , likely nonlinearly generated, become significant for $TI \geq 2.4\%$, as demonstrated in figure 7. Figure 8(j,k,l) shows the evolution of $|u'|$ with the streamwise Reynolds number $Re_x^{1/2}$ ($\propto Re_{\delta^*}$). In most cases, there is a region with a linear trend in the curves, indicating proportionality between $|u'|$ and $Re_x^{1/2}$, which is characteristic of the growth of streaks (Luchini 2000). This linear trend becomes less pronounced for increasing TI , suggesting that the influence of transient growth lessens.

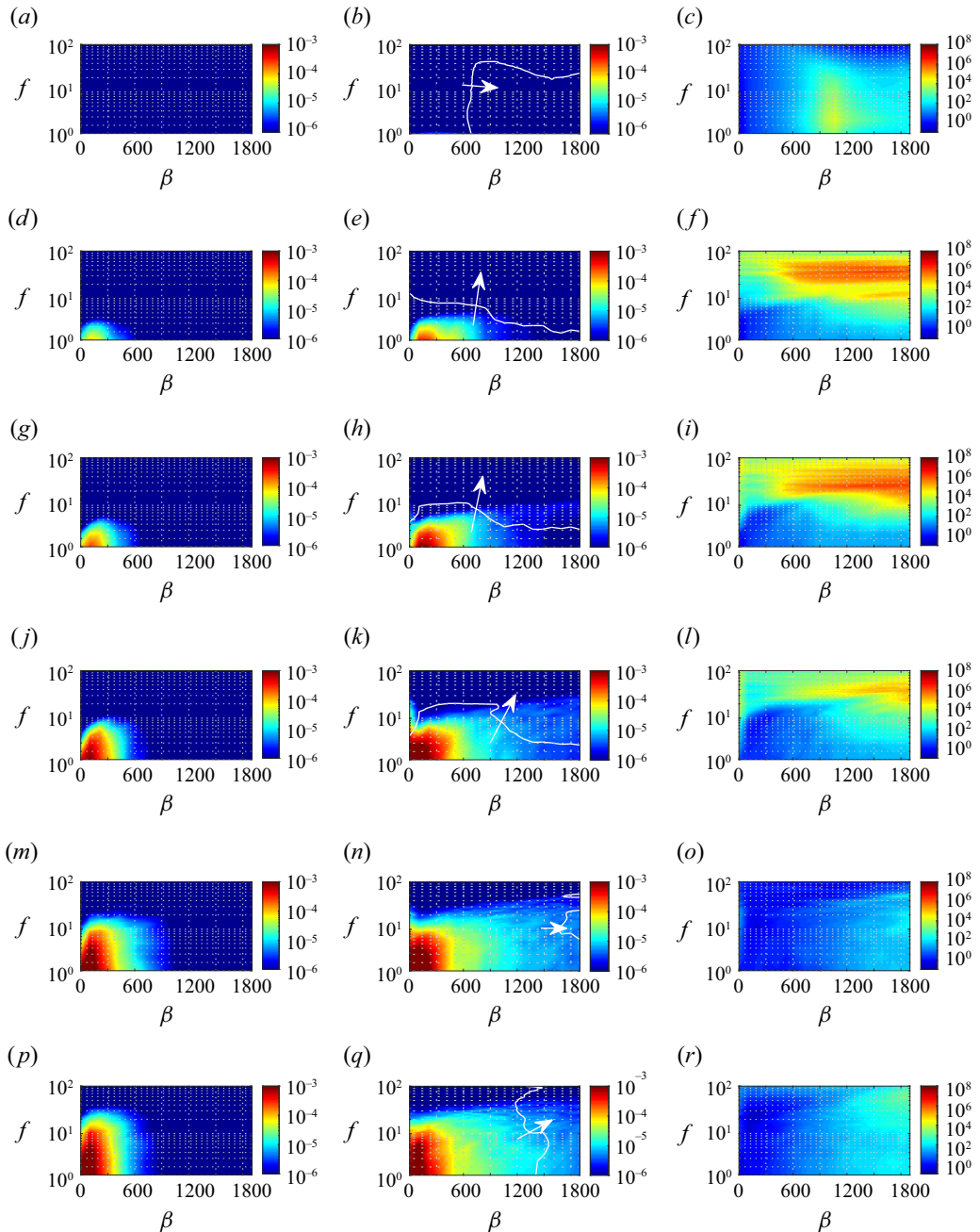


Figure 7. Spectra of perturbation kinetic energy at $y = 120\delta^*$ ($|k'_{120\delta^*}|$, left column), $y = \delta^*$ ($|k'_{\delta^*}|$, centre column) and $|k'_{\delta^*}|/|k'_{120\delta^*}|$ (right column) at the leading edge ($x = 0$) for (a,b,c) $TI = 0\%$, (d,e,f) 0.6% , (g,h,i) 1.2% , (j,k,l) 2.4% , (m,n,o) 4.5% and (p,q,r) 7% . The white isoline in the centre column indicates $|k'_{\delta^*}|/|k'_{120\delta^*}| = 100$ and the arrow indicates the region with $|k'_{\delta^*}|/|k'_{120\delta^*}| > 100$.

3.3. Disturbance evolution and flow stability

3.3.1. Transition to turbulence

Estimations of the mean transition location (x_{tr}) based on the maximum boundary layer shape factor (H) are not accurate here as H does not reach a maximum upon transition,

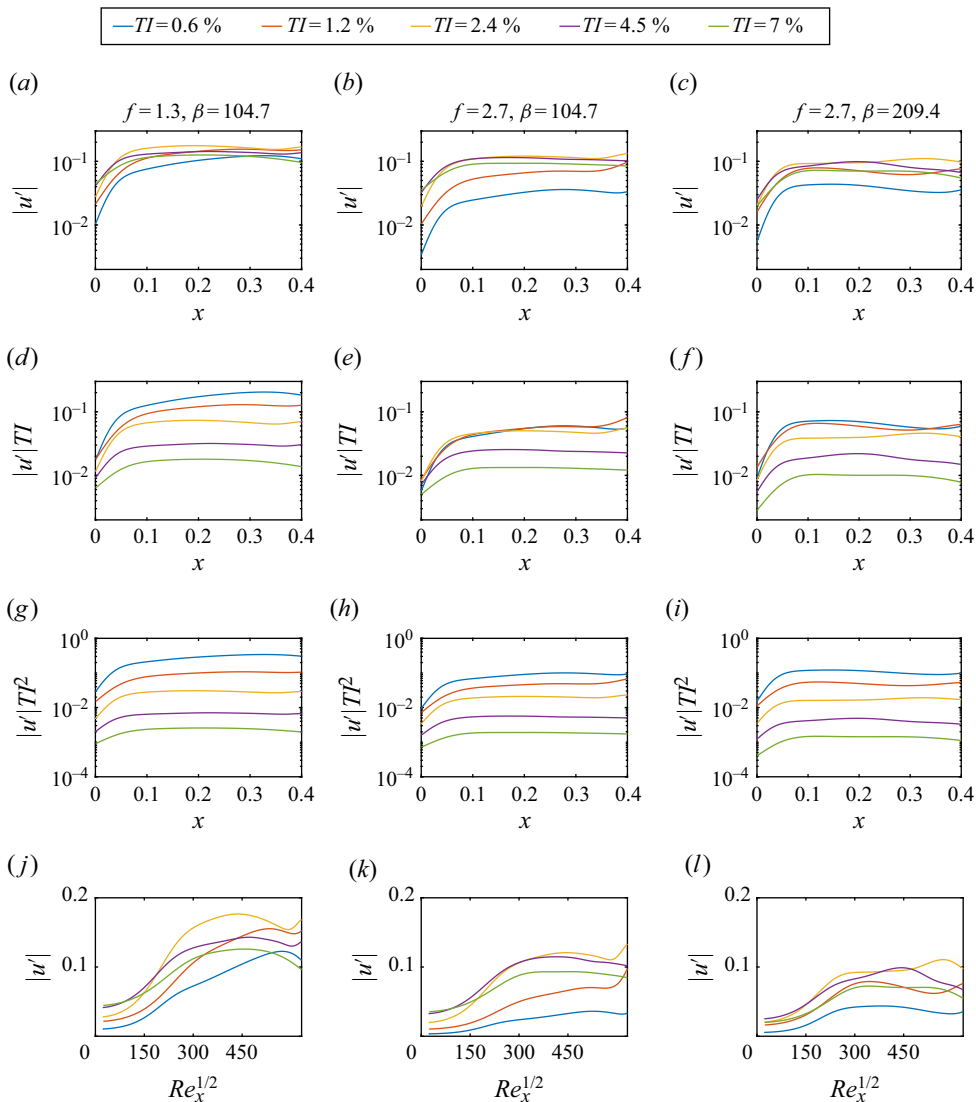


Figure 8. Streamwise evolution of the wall-normal maximum inside the boundary layer of the (a,b,c) streamwise velocity fluctuations ($|u'|$), (d,e,f) $|u'|/TI$, (g,h,i) $|u'|/TI^2$. (j,k,l) Evolution of $|u'|$ as a function of $Re_x^{1/2}$.

TI	0 %	0.6 %	1.2 %	2.4 %	4.5 %	7 %
$\max_x \langle u'_{rms} \rangle_z / U_\infty$	0.213	0.244	0.260	0.247	0.223	0.222
$\max_x \langle u'_{rms} \rangle_z / u_e$	0.176	0.185	0.186	0.172	0.156	0.150
$x_{lr1} = \arg \max_x \langle u'_{rms} \rangle_z$	0.554	0.505	0.459	0.421	0.417	0.302
$\max_x \max_z u'_{rms} / U_\infty$	0.264	0.286	0.301	0.286	0.261	0.250
$\max_x \max_z u'_{rms} / u_e$	0.198	0.206	0.213	0.197	0.180	0.172
$x_{lr2} = \arg \max_x \max_z u'_{rms}$	0.558	0.500	0.463	0.404	0.374	0.366
$x_{lr3} = (1/2)(\arg \min_x c_f + \arg \max_x c_f)$	0.565	0.498	0.456	0.417	0.403	0.339

Table 2. Mean transition locations.

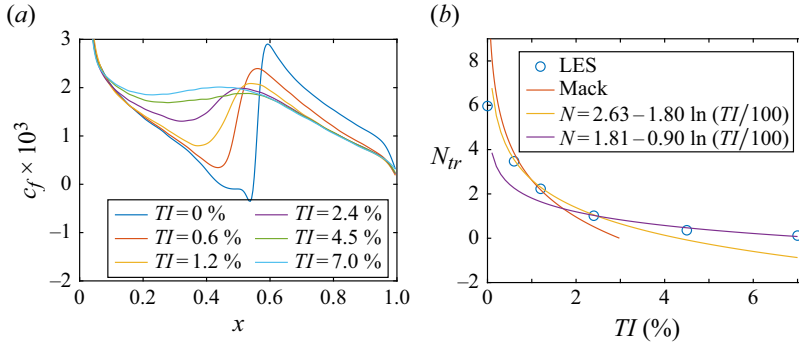


Figure 9. (a) Mean friction coefficient (c_f). (b) Critical N factor (N_{tr}).

unlike in other works (Fava *et al.* 2023c), especially for high TI . Three criteria are considered for estimating x_{tr} . The first two consider it the x locus of maximum $\langle u'_{rms} \rangle_z$ (x_{tr1}) and $\max_z u'_{rms}$ (x_{tr2}). The results summarised in table 2 indicate small differences between the two methods for $TI \leq 1.2\%$. Due to the increased occurrence of spanwise-localised instabilities, $x_{tr1} > x_{tr2}$ for $TI = 2.4\% - 4.5\%$ as the transition line becomes very spanwise inhomogeneous (see figure 4e). Nevertheless, $x_{tr1} < x_{tr2}$ for $TI = 7\%$ since the elevated number of streaks promotes the spanwise homogeneity of the transition line, reducing the probability of a single streak reaching a high amplitude before the onset of the breakdown (see figure 4f). The disturbance amplitude at x_{tr} is also listed in table 2, normalised by U_∞ and the local edge velocity (u_e). The maximum amplitude of $0.260U_\infty$ (mean) or $0.301U_\infty$ (maximum) occurs for $TI = 1.2\%$, the highest TI for which the mean flow is unstable to TS waves. Interestingly, $0.260U_\infty$ corresponds to the threshold for the occurrence of an outer secondary instability of the streaks in Blasius flow (Andersson *et al.* 2001). Hack & Zaki (2014) reported $u'_{rms} = 0.16u_e$ before the breakdown of the streaks, close to the values obtained at x_{tr1} for $TI \geq 2.4\%$. Finally, the last criterion for estimating x_{tr} relies on computing the friction coefficient (c_f), shown in figure 9(a), and assuming $x_{tr3} = (1/2)(\arg \min_x c_f + \arg \max_x c_f)$. The rationale is that c_f grows rapidly upon transition. The c_f in the leading edge region was excluded since its high values are unrelated to transition. The values obtained with this method are close to x_{tr1} , except for $TI = 7\%$. In the remainder of the paper, $x_{tr} = x_{tr1}$.

Figure 9(b) portrays the critical N factor ($N_{tr} = N(x_{tr})$) as a function of TI , defined as $N_{tr} = \ln(\max_y \langle k'_{rms} \rangle_z / \max_y \langle k'_{rms0} \rangle_z)$, where $k'_{rms0} = k'_{rms}(x_0)$, $x_0 = 4 \times 10^{-3}$. Similar to Mack (1977), this definition of N_{tr} encompasses perturbations unrelated to transition, unlike the N factor obtained from linear stability theory. However, these two definitions should be close for transition dominated by TS waves, as the disturbances related to the latter tend to stand out above the background noise for low TI . The figure shows that the N factor drops rapidly with TI for $TI \leq 2.4\%$, with a trend well predicted by Mack's correlation (1.3) (Mack 1977). The exception is $TI = 0\%$, whose N_{tr} is lower than predicted due to flow separation. Mack's correlation relies on experimental data from zero pressure gradient flat plates under grid turbulence. The close agreement is surprising since the pressure gradient, curvature and FST spectra differ from the experiments. Linear regression of a correlation of the form $N_{tr} = a - b \ln(TI/100)$ to the $TI \leq 2.4\%$ data yields $a = 2.63$ and $b = 1.8$ with errors $\sigma_a = 0.51$ and $\sigma_b = 0.11$. Appendix A presents details of these calculations. This allows a better fit to the LES data as the expression presents a less steep slope than Mack's correlation. The low and slightly dropping N factor obtained from the LES for $TI > 2.4\%$ indicates bypass transition. The expression

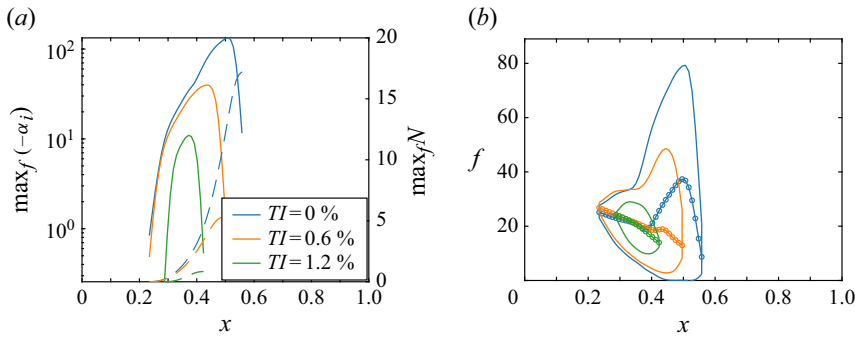


Figure 10. Local spatial stability analysis results for $\beta = 0$. (a) Frequency envelope of growth rates (solid lines) and N factor (dashed lines). (b) Neutral curve, where $-o-$ indicates the most unstable frequency.

that best fits the $2.4\% \leq TI \leq 7\%$ region has coefficients $a = 1.81$ and $b = 0.9$ with errors $\sigma_a = 0.50$ and $\sigma_b = 0.16$. Unlike the expression obtained for $TI \leq 2.4\%$, which, together with linear stability theory and the e^N method, can be used for estimating the transition location, the correlation for $2.4\% \leq TI \leq 7\%$ is merely an indication of the gain of the perturbations in bypass transition. Interestingly, the coefficient b for $2.4\% \leq TI \leq 7\%$ is half that for $TI \leq 2.4\%$. Note that each correlation was obtained with three data points. A comparison with more data is needed to assess their validity further.

3.3.2. Primary instability and disturbance growth

Local linear stability theory (LST) is employed to help interpret the nonlinear simulations. The formulation of Fava *et al.* (2023c) is employed where the ansatz $\phi' = \hat{\phi}(y) \exp(-i\alpha x + i\omega t + i\beta z)$ is inserted in the linearised Navier–Stokes equations, with a parallel-flow hypothesis, and solved for $\hat{\phi}$ and $\alpha = \alpha_r + i\alpha_i$. Here, ϕ' represents pressure and velocity disturbances for given $\omega = 2\pi f$ and β ; α_r is the streamwise wavenumber; and α_i is the growth rate. The base flow is the spanwise- and time-averaged field for each TI . Analyses are only performed for $\beta = 0$ ($n_z = 0$) since these are the most unstable modes in two-dimensional flows (Squire 1933), as those for low TI .

Unstable modes with positive group velocity exist. Figure 10(a) presents their frequency envelope of growth rates (solid lines) and N factors (dashed lines). The maximum amplification occurs on average 6% chord upstream of the transition locations and decreases with TI due to the spanwise-averaged part of the mean-flow distortion, a phenomenon observed in experiments (Boiko *et al.* 1994; Fransson *et al.* 2005) and simulations (Fasel 2002; Fava *et al.* 2023b). This effect stabilises the mean flow with respect to two-dimensional TS waves for $TI \geq 2.4\%$, suggesting that the instability of streaks becomes the dominant transition trigger in this range. However, the streaks may have an impact on the growth of the TS waves for lower TI , distorting the wavefronts and triggering their secondary instability (Kendall 1990; Liu *et al.* 2008; Vaughan & Zaki 2011; Hosseini-verdi & Fasel 2019). This analysis requires the consideration of the spanwise variation of the flow due to the streaks, which is performed in § 3.3.3. The neutral curves in figure 10(b) indicate that the frequency of the most unstable TS waves is little affected by TI upstream of flow separation. The latter occurs for $TI = 0\%$, leading to the inception of KH modes and a rise in the frequency of the most unstable modes. This differs from the $Re_c = 10^5$ case, where the KH modes have a lower frequency than the TS waves (Fava *et al.* 2023c). Another reason for the agreement between the neutral curves for $x < 0.4$ is

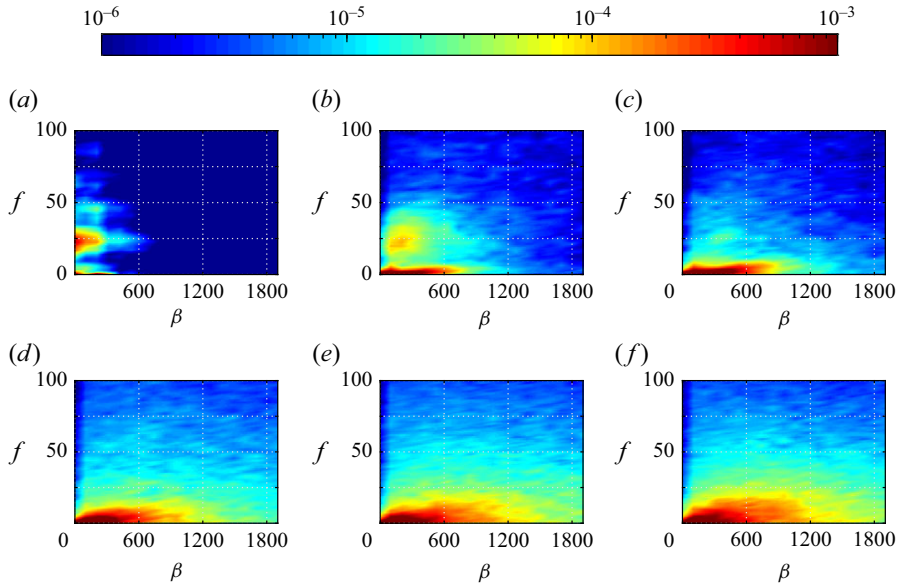


Figure 11. Spectra of perturbation kinetic energy at $y = \delta^*$ from LES for (a) $TI = 0\%$ at $x = 0.53$, (b) $TI = 0.6\%$ at $x = 0.46$, (c) $TI = 1.2\%$ at $x = 0.4$, (d) $TI = 2.4\%$ at $x = 0.38$, (e) $TI = 4.5\%$ at $x = 0.35$ and (f) $TI = 7\%$ at $x = 0.3$.

the low MFD in this region (see [figure 2](#)). The range of unstable TS waves narrows for $TI = 1.2\%$ as the mean flow loses its inflectional character.

[Figure 11](#) shows the perturbation kinetic energy spectra close to transition. For $TI = 0\%$, there are high-amplitude disturbances centred around $f = 22.9$ and $\beta = 0$, as shown in [figure 11\(a\)](#). The maximum N factor obtained from LST occurs exactly at this frequency, which is a good indication that they represent the same modes, namely inflectional instabilities of the separated shear layer (KH modes). Triadic interactions (Craik 1971) between the fundamental ($f = 22.9$, $\beta = 0$), oblique ($f = 22.9$, $\beta = 209.4$) and streaky ($f = 0$, $\beta = 209.4$) modes may be a relevant mechanism due to the observed high amplitude of the fundamental and streaky disturbances. This can correspond to the oblique mechanism described by Marxen *et al.* (2003) and observed by Fava *et al.* (2024a), which leads to a rapid transition to turbulence, as seen in [figure 4\(a\)](#). The spectrum also shows the excitation of frequency harmonics of the fundamental instability, particularly at $f = 2f_f = 45.8$. Considering $TI = 0.6\%$ in [figure 11\(b\)](#), disturbances centred around $f = 22.9$ present high amplitude, similar to $TI = 0\%$. However, unlike the latter, a larger magnitude occurs for $\beta = 209.4$ instead of $\beta = 0$. This is expected as separation is suppressed, reducing the growth rates of 2-D inflectional instabilities, while streaks develop a high amplitude. Disturbances with $f = 0$, $\beta = 209.4$ also display high amplitude. These facts parallel the $TI = 0\%$ case and may indicate that vortical disturbances penetrating the boundary layer further excite the oblique mechanism. This mechanism is also possibly present for $TI = 1.2\%$. Although the mean flow is not inflectional, it is unstable to TS waves, as demonstrated with LST, and a region with a large amplitude is present in the spectrum ([figure 11c](#)) near the predicted frequency of these waves and at the same β of the highest amplitude stationary disturbances, related to streaks. Further rises in TI ([figure 11d,e,f](#)) stabilise two-dimensional disturbances associated with TS waves, and consequently oblique disturbances generated by nonlinear

interactions between TS waves and streaks. High-amplitude disturbances are concentrated at low frequencies, corresponding to streaks.

The most energetic structures are extracted with spectral proper orthogonal decomposition (SPOD) of the velocity perturbations (Lumley 1970; Towne *et al.* 2018; Schmidt & Colonius 2020). The streaming SPOD algorithm of Schmidt & Towne (2019) is employed, reducing memory requirements as it is unnecessary to store all snapshots simultaneously. The data involve 6600 snapshots with a time step of 9×10^{-4} (Nyquist frequency $f = 555.6$). The snapshots are split into five blocks (five computed SPOD modes) with 50 % overlap and a Hamming window. The weight matrix is the distance between two consecutive wall-normal grid points, and the employed norm measures k' integrated over the xy plane (Schmidt & Towne 2019). The analysed domain stretches from the leading edge ($x = 0$) to x_{tr} , excluding the turbulent flow region from the SPOD.

The occurrence of modal instabilities (e.g. TS and KH modes) is assessed in figure 12, which shows the isocontours of the real part of the first SPOD mode of streamwise velocity perturbation for $f = 22.8$, $\beta = 0$ in the left column. These results are compared with those obtained with the parabolised stability equations (PSEs) of Fava *et al.* (2023a,b), shown in the right column. This PSE formulation allows for a streaky base flow and interactions between the streaks and modal instabilities. Such capacity is only used for $TI = 2.4$ %, where a perturbation expansion with $N_s = 4$ spanwise harmonics is considered, and the base flow is a superposition of the spanwise- and time-averaged flow and steady streaks with $\beta = 104.7$, $A_u = 10$ % U_∞ . Figure 12(h) shows the streak profile. In the other cases, the spanwise- and time-averaged flow is assumed to be the base flow and $N_s = 0$, retrieving the standard PSE of Herbert (1997). Figure 12(a) shows the results for $TI = 0$ %, indicating the formation of TS waves upstream of the LSB (green line). Near the maximum LSB height, the structure displays a high amplitude lobe inside the LSB, a second lobe at δ^* (black line) and a third lobe above the latter. This indicates a KH mode well predicted by the PSE in figure 12(b). The SPOD mode for $TI = 0.6$ % in figure 12(c) indicates an inflectional TS mode with a local maximum at the inflection point location ($y = \delta^*$) and another further away towards the free stream. The PSE result agrees well with this mode, as shown in figure 12(d). In the $TI = 1.2$ % case in figure 12(e), there is only a region with high amplitude (near-wall lobe) close to the end of the domain (transition location). The PSE predicts a decaying TS wave, as depicted in figure 12(f), which is unsurprising as the mean flow is not inflectional. The $TI = 2.4$ % case is stable to TS waves, considering only the mean flow. Nevertheless, a wavepacket resembling an inflectional TS wave appears in the SPOD mode in figure 12(g). The consideration of a streaky base flow in the PSE, as discussed above, enables an instability with a low near-wall maximum and peak amplitude at the inflection point generated by the base streak, as shown in figure 12(h). This mode seems to display mixed contributions from inner and outer modes, with a predominant contribution from the former for the $TI = 1.2$ % case and the latter for $TI = 2.4$ %.

Figure 13 shows the isocontours of the gain G for steady disturbances from LES, defined as $G = E/E_0$, where $E = \int_0^{y_{max}} k'(x, y, \beta, f) dy$, $E_0 = E(x_0)$ and y_{max} is the wall-normal location of the boundary layer edge. Here, G displays low sensitivity to x_0 for the values assessed and $x_0 = 0.005$ is selected. The norm E is similar to that of optimal perturbation analysis (OPA) (Andersson *et al.* 1999; Luchini 2000), which is applied assuming that the mean flow of the $TI = 0$ % case is the base flow where the streaks grow. The isolines of G from OPA are presented in figure 13(a) with the isocontours of G from LES for $TI = 0$ %. This panel shows a region of high G near the leading edge with an initial $\beta \approx 1500$, which decays with x . This region can be associated with

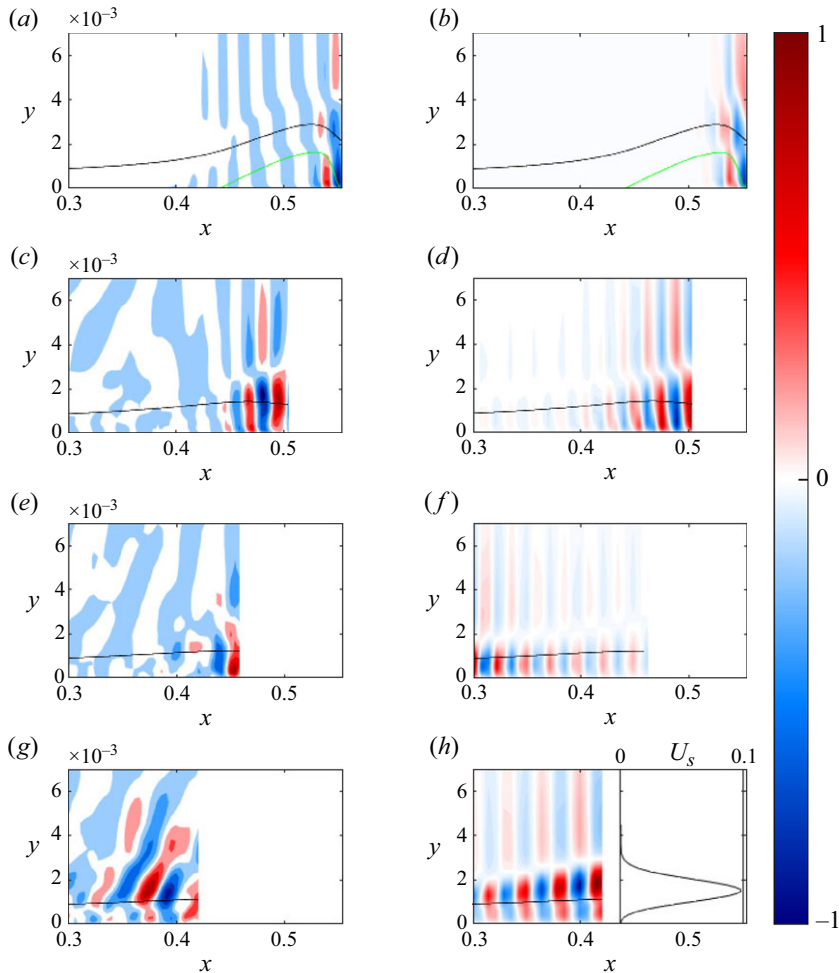


Figure 12. Real part of the first SPOD mode of streamwise velocity perturbation (normalised) for $f = 22.8$, $\beta = 0$ for (a) $TI = 0\%$, (c) $TI = 0.6\%$, (e) $TI = 1.2\%$, and (g) $TI = 2.4\%$. PSE results are shown in panels (b), (d), (f) and (h). For $TI = 2.4\%$, the PSE base flow contains a u' -fluctuation with $f = 0$, $\beta = 104.7$, $A_u = 10\%U_\infty$ with profile U_s shown in panel (h). The black and green lines indicate δ^* and the LSB edge.

the growth of streaks due to the lift-up effect. The maximum $G \approx 10$ agrees with that predicted by OPA for $\beta = 1256.6$ at $x = 0.07$. OPA reaches $G = O(10^{12})$ for $\beta = 2722.7$ further downstream, as also found by Cherubini *et al.* (2010), due to a high degree of non-normality of the linearised Navier–Stokes operator. Nevertheless, these gains are not attained in the LES. Note that the fact that there is non-modal growth in the $TI = 0\%$ case does not mean that streaks participate in the transition process since the background noise is very low. The $TI = 0.6\%$, 1.2% and 2.4% cases in figure 13(b,c,d) also indicate streak growth. The maximum G is considerably reduced for $TI = 2.4\%$ and nearly vanishes for $TI = 4.5\%$ and 7% in figure 13(e,f). This suggests that the streaks barely grow due to the lift-up effect for $TI > 2.4\%$ since the FST already induces streaks with a large amplitude near the leading edge. This highlights why the perturbation amplitude in the boundary layer scales linearly with TI for $TI \leq 2.4\%$ but sub-linearly otherwise. Lastly, the $TI \leq 1.2\%$ cases present a high gain of $\beta = 0$ disturbances near the mid-chord region due to two-dimensional modal instabilities, absent for higher TI .

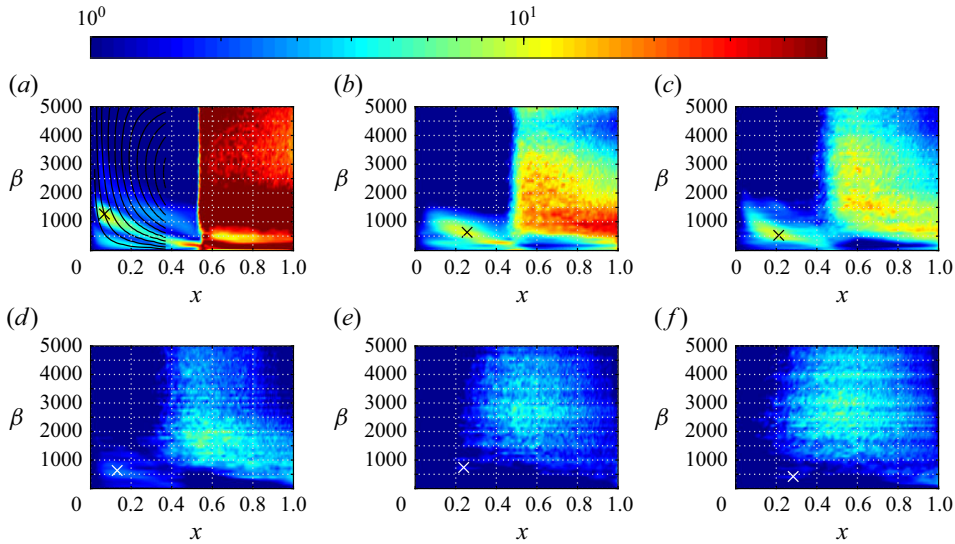


Figure 13. Perturbation kinetic energy gain (maximum in the wall-normal direction) from LES for $f = 0$ and (a) $TI = 0\%$, (b) $TI = 0.6\%$, (c) $TI = 1.2\%$, (d) $TI = 2.4\%$, (e) $TI = 4.5\%$ and (f) $TI = 7\%$. The \times markers indicate the (x, β) of the maximum gain of the streaks. The isolines of gain obtained from OPA are shown in black for $(1, 10, 100, \dots)$.

Figure 14 compares the evolution of $|u'|$ from LES and OPA. The latter is a linear method, and its results are scaled to match the amplitude of the $TI = 0.6\%$ case at a given x . There is good agreement between the two methods, considering the initial streak growth. This agreement improves with increasing f and decreasing β , as shown in figure 14(g), where there is a close match until $x = 0.2$. In general, OPA also predicts well the streak growth for $TI \leq 2.4\%$ (the scaled OPA curves for $TI = 1.2\%$ and 2.4% are not shown for a cleaner figure). The agreement between OPA and LES is worse for $TI = 4.5\%$ and 7% , since the latter displays slower growth, suggesting that the lift-up may not be the leading mechanism of streak generation in these cases. Note that the amplitude obtained from OPA keeps growing downstream, whereas that from LES saturates. Figure 15 also indicates close agreement between the $|u'|$ profiles from LES and OPA at $x = 0.2$. The agreement reduces towards the free stream as the LES profiles present a higher amplitude than those from OPA due to the influence of FST.

3.3.3. Secondary instability and breakdown of streaks

Typical events of instability and nucleation of turbulent spots are studied. Figure 16 shows the Q -criterion isosurfaces at time $T = 0$ and $T = 0.1$, preceding and during the turbulent breakdown. The earliest breakdown for $TI = 1.2\%$ occurs on a streak near $z = 0$ at $T = 0$ with a wavepacket present in the region denoted by W in figure 16(a). The streaks travel at a speed $u_s \approx 0.67u_e$, close to the value of Vaughan & Zaki (2011). Since $u_s \approx 1$, the streak is $\Delta x \approx 0.1$ more downstream at $T = 0.1$ in figure 16(b), where the turbulent spot develops. The rear location of the wavepacket is fixed at $x = 0.38$, while the streak travels through this point. This suggests an influence of TS waves on the streak breakdown since they reach maximum growth at this location, as depicted in figure 10(a). As seen in other regions along the span, TS waves without streaks lead to a downstream breakdown. The wavepacket disappears after the rear of the streak crosses $x = 0.38$. For $TI = 2.4\%$, figure 16(c) shows a pair of streaks at $z = 0.055$ at $T = 0$,

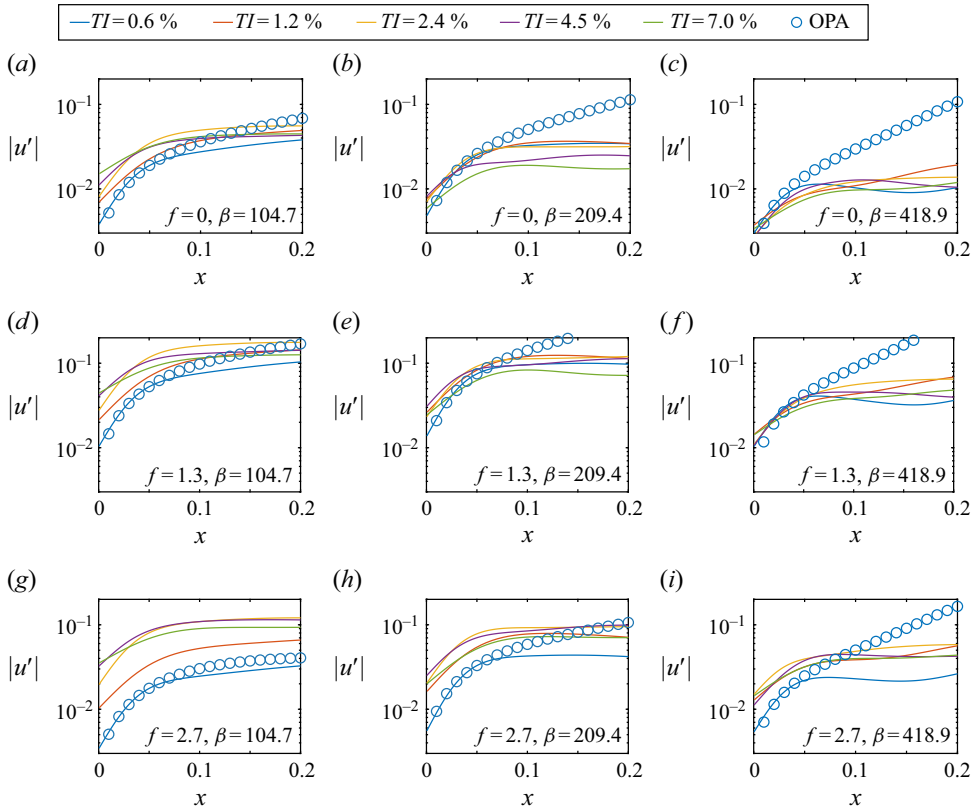


Figure 14. Wall-normal maximum of the absolute value of streamwise velocity perturbation computed with LES (solid lines) and OPA (circles).

with the streamwise location of their trailing edge marked with a grey line. [Figure 16\(d\)](#) indicates that they evolve into a wavepacket downstream of $x = 0.27$ at $T = 0.1$, suggesting a secondary instability of this dual configuration. The turbulence spot is significantly more upstream than the breakdown in other regions along the span. Regarding $TI = 4.5\%$, streaks centred at $z = 0.04$ at $T = 0$ undergo turbulent breakdown of conical shape at $T = 0.1$, as shown in [figures 16\(e\) and 16\(f\)](#). This case presents many narrow streaks, seemingly more susceptible to breakdown, and an elevated spanwise non-uniformity in the transition line.

[Figure 17](#) displays the structures of the modes analysed in [figure 16](#). For $TI = 1.2\%$ in [figure 17\(a\)](#), a low-speed streak (grey) lies on the flank of a high-speed streak (black). The former eventually goes above the latter, triggering an instability in the low-speed streak, characterised by spanwise waves. This may indicate TS waves triggered by the wall-normal shear created by the streaks since the mean flow is only weakly unstable. The configuration evolves to a delta shape at the junction of high- and low-speed streaks, characteristic of inner modes ([Nagarajan et al. 2007](#); [Vaughan & Zaki 2011](#)), which are predominantly of the varicose type ([Dotto et al. 2022](#)). Even though the overview of the mode structure indicates an inner mode, analyses of the perturbation profiles at $x = 0.38$, $z = 0.03$ suggest that the wavepacket responsible for the early breakdown in [figure 16\(a\)](#) is an outer mode. This indicates that the inner mode is present more upstream, while the outer mode dominates at the transition point. Regarding $TI = 2.4\%$, [figure 17\(b\)](#) shows that a low-speed streak is beneath a high-speed streak. As the former rises to the top of the

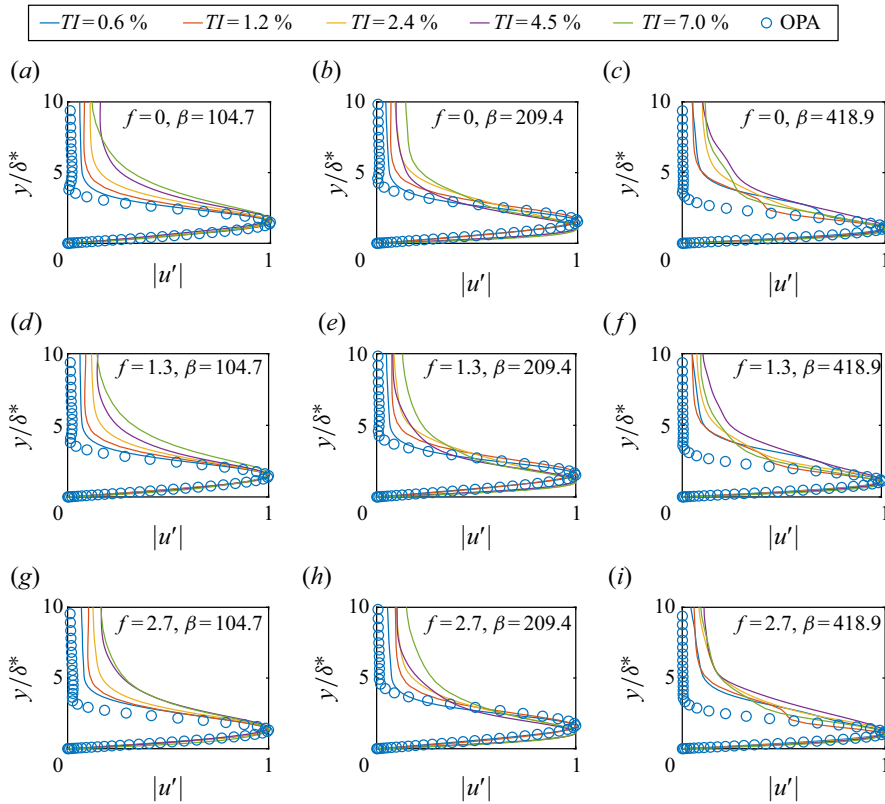


Figure 15. Wall-normal profiles of the absolute value of streamwise velocity perturbation (normalised by the maximum) computed with LES (solid lines) and OPA (circles) at $x = 0.2$.

boundary layer, an outer varicose instability occurs over the low-speed streak, as shown by Brandt *et al.* (2004). Structures similar to lambda vortices appear and give rise to a turbulent spot (Perry *et al.* 1981; Dotto *et al.* 2022). Figure 17(c) presents the results for $TI = 4.5\%$, where a low-speed streak has high-speed streaks on both flanks and beneath it. The low-speed streak develops oscillations in the spanwise and wall-normal directions, corresponding to an outer sinuous instability according to Brandt *et al.* (2004). The latter typically occurs due to the spanwise shear and inflection point. The low-speed streaks break down first in all cases.

The secondary stability analysis over cross-sectional planes of the instantaneous flows preceding the breakdowns discussed above follows Siconolfi *et al.* (2015). A 2-D, local eigenvalue problem is justified as the streamwise flow variations are much slower than those in the wall-normal and spanwise directions. The spatial approach was employed, where downstream-propagating waves with a frequency $f \in \mathbb{R}$ are amplified with spatial growth rate $-\alpha_i$. Appendix B presents further details. Figure 18(a) shows the time evolution of the growth rates at $x = 0.4$ for $TI = 1.2\%$. This location is near the wavepacket trailing edge, fixed in space while the streak travels. The growth rates increase with time until $T = 0$, followed by a drop due to the ensuing transition. Figure 18(b) presents the spectrum of perturbation kinetic energy from the LES at $x = 0.4$ for $TI = 1.2\%$ and indicates energetic disturbances close to the frequency predicted by the secondary stability analysis (LST) at peak amplification ($f = 120$) at $T = 0$.

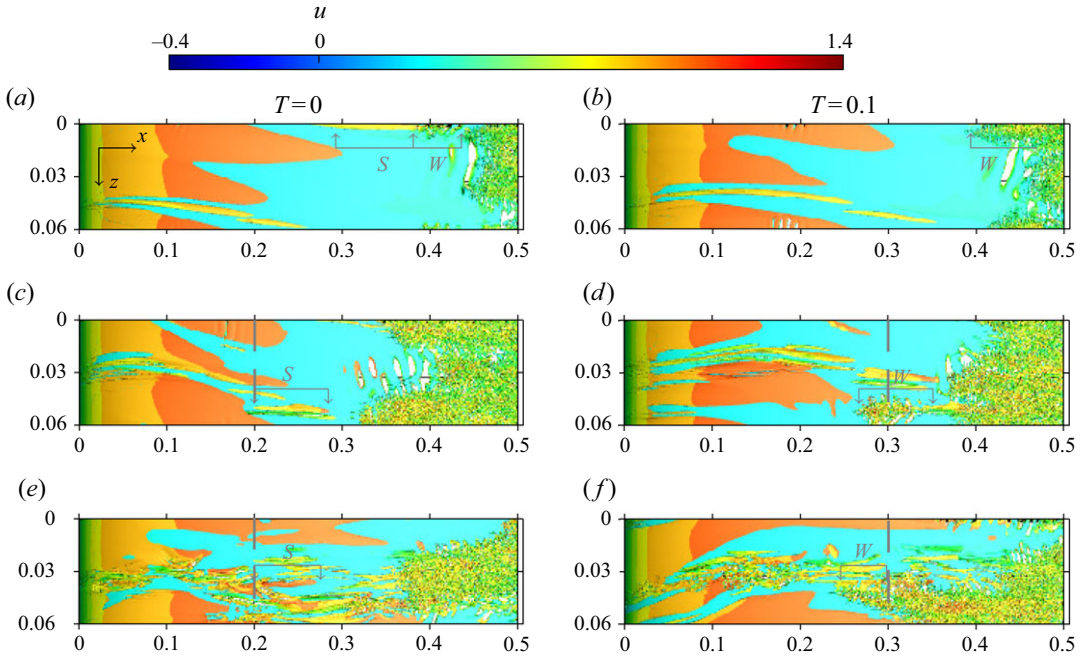


Figure 16. Analysis of a typical turbulent breakdown of streaks for (a,b) $TI = 1.2\%$, (c,d) $TI = 2.4\%$ and (e,f) $TI = 4.5\%$ visualised with the isosurfaces of Q -criterion ($Q = 100$) coloured by the instantaneous streamwise velocity. T is the relative time between snapshots and $T = 0$ means different initial times for each TI . The wavepackets and streaks are shown with the symbols W and S . The grey lines in panel (c,d,e,f) indicate the streamwise location of the rear end of the analysed streak.

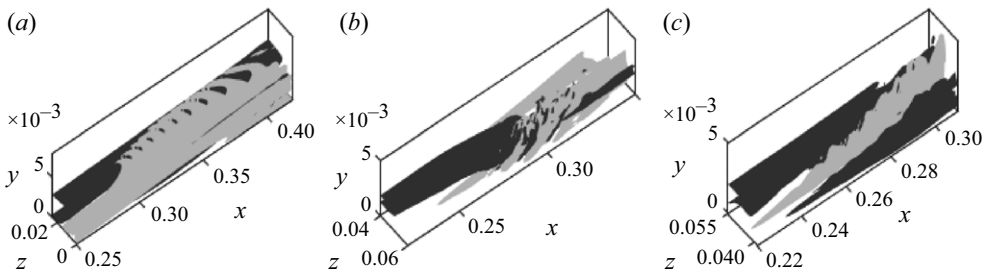


Figure 17. Isosurfaces of streamwise velocity fluctuations showing the instabilities in figure 16. The positive and negative fluctuations are shown in black and grey: (a) $TI = 1.2\%$ at $T = 0$ with $u' = \pm 0.03$; (b) $TI = 2.4\%$ at $T = 0.1$ with $u' = (-0.1, 0.12)$; (c) $TI = 4.5\%$ at $T = 0.1$ with $u' = (-0.15, 0.09)$. The z -axis direction in panel (b) is reversed compared with that in panels (a) and (c).

Figure 18(c) exhibits the growth rates on a plane travelling with the streak for $TI = 2.4\%$. The amplification increases as the streak moves downstream, with an exceptionally high value at $x = 0.3$, $T = 0.1$, where the most unstable mode frequency drops, suggesting a mechanism change compared with more upstream locations. The spectrum in figure 18(d) displays several regions with highly energetic disturbances near the frequency of peak amplification ($f = 120$) at $x = 0.3$, $T = 0.1$. Figure 18(e) portrays the growth rates for $TI = 4.5\%$, revealing a rise in amplification as the streaks move downstream. At $x = 0.3$, $T = 0.1$, the frequency of the most unstable mode is $f = 115$, which also lies near regions with high energy in the spectrum in figure 18(f). The fact that the frequencies of the most

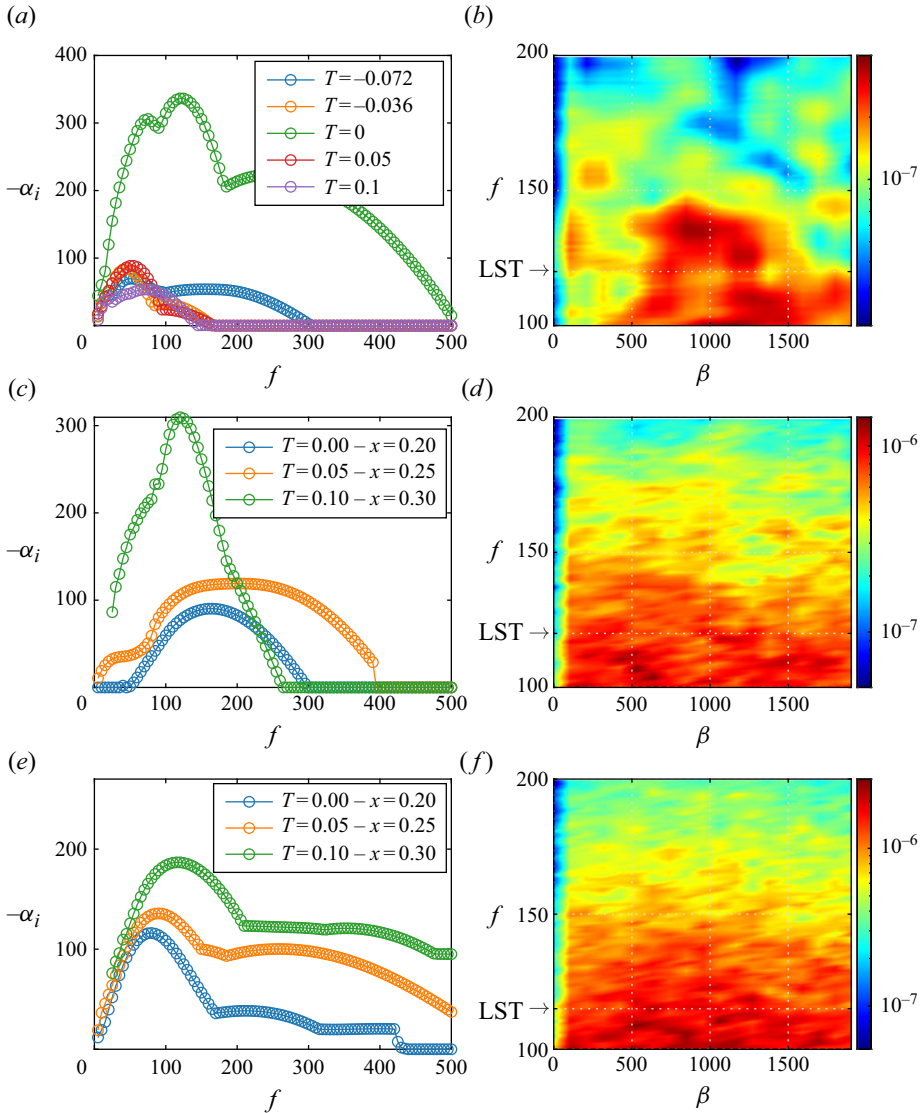


Figure 18. Time evolution of the growth rates obtained with cross-sectional secondary linear stability theory (LST) (a) at $x = 0.4$ for $TI = 1.2\%$, and following a streak for (c) $TI = 2.4\%$ and (e) $TI = 4.5\%$. Spectra of perturbation kinetic energy at $y = \delta^*$ from LES (b) at $x = 0.4$ for $TI = 1.2\%$, and at $x = 0.3$ for (d) $TI = 2.4\%$ and (f) $TI = 4.5\%$.

unstable modes in the stability analysis lie close to regions with high energy in the LES spectrum suggests that the investigated breakdowns may be general events.

Figure 19 shows the comparison between the profiles of the streamwise velocity perturbations extracted from the LES and those predicted by secondary stability analysis, considering the most unstable mode at each location and time. Panel (a) presents the results for $TI = 1.2\%$. At $T = -0.25$, the profile at $x = 0.13$ indicates a streak, whereas that at $x = 0.38$ corresponds to a TS wave, well predicted by LST. This streak arrives at $x = 0.38$ at $T = 0$, where the profile displays the characteristics of an outer mode in agreement with that obtained with secondary stability analysis for $f = 120$. The phase

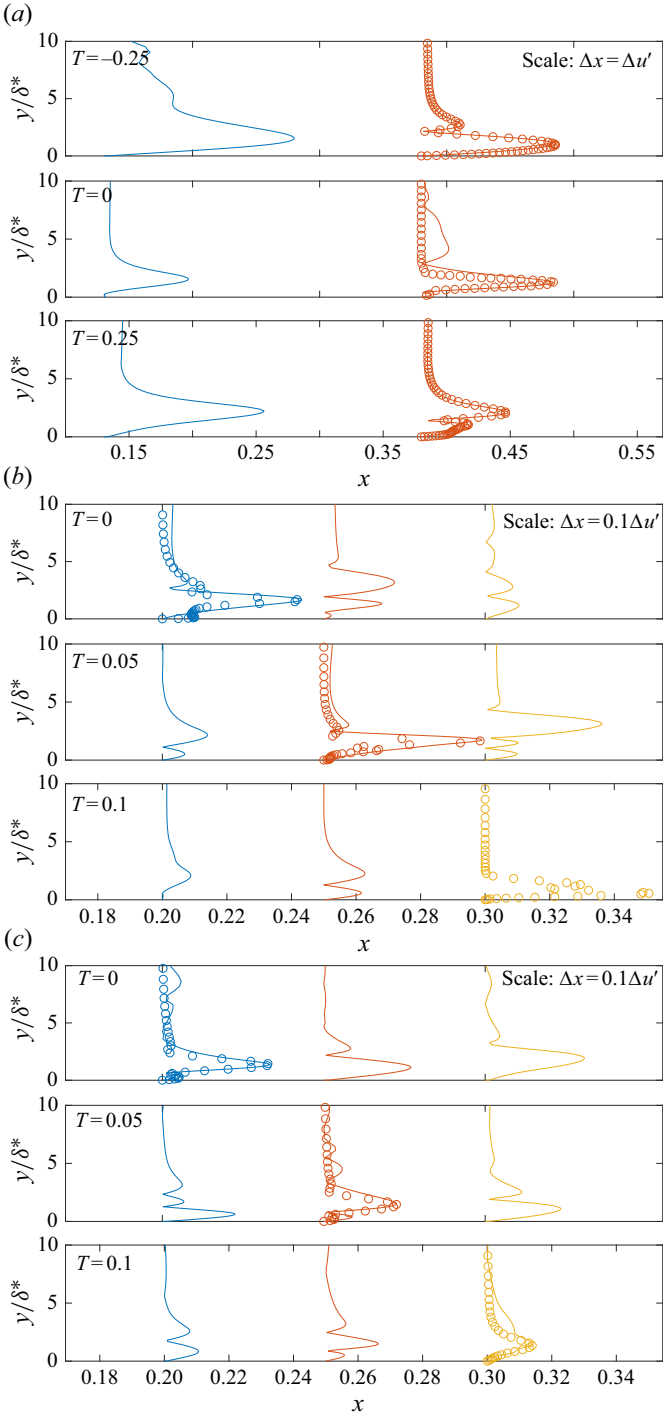


Figure 19. Wall-normal profiles of the absolute value of streamwise velocity perturbation computed with LES (solid lines) and secondary stability analysis over the cross-planes considering the most unstable frequency (circles) at (a) $z = 0.005$ for $TI = 1.2\%$, (b) $z = 0.052$ for $TI = 2.4\%$ and (c) $z = 0.041$ for $TI = 4.5\%$.

speed is $c_p = 0.73 u_e$, close to the $c_p = 0.75 u_e$ value obtained by Vaughan & Zaki (2011) for outer modes. Moreover, the peak amplitude occurs at the location of the inflection point in the wall-normal profile of streamwise velocity, indicating that this instability is of the varicose type. Less amplified modes in the secondary stability analysis present $c_p = 0.54 u_e$, which agrees with the phase speed of inner modes by Vaughan & Zaki (2011). The streak has a lower initial amplitude at $x = 0.13$, $T = 0$. In this case, the mode at $x = 0.38$, $T = 0.25$ presents an increased near-wall maximum due to the inner mode contribution and a reduced maximum due to the outer mode contribution.

Figure 19(b) presents the results for $TI = 2.4\%$. At $x = 0.2$, $T = 0$, and $x = 0.25$, $T = 0.05$, the perturbation profiles correspond to outer modes. The secondary stability results predict these modes well and indicate a phase speed $c_p = 0.69 u_e$, in the range the literature provides for outer modes. The maximum amplitude occurs near the location of the maximum wall-normal shear and inflection point ($y/\delta^* = 1.6$), which lie on the low-speed streak. Although the spanwise inflection point is near the mode maximum amplitude location, the spanwise shear is low compared with the wall-normal shear. These facts suggest a varicose type of instability. However, the mode characteristics change considerably at $x = 0.3$, $T = 0.1$, where the peak amplitude moves closer to the wall ($y/\delta^* = 0.56$), and the frequency of the most unstable mode according to LST drops relative to the outer modes upstream. The profile and phase speed $c_p = 0.54 u_e$ are typical of an inner mode (Vaughan & Zaki 2011). The inner mode at $x = 0.3$, $T = 0.1$ is driven by the spanwise shear and presents a maximum amplitude at the location of the inflection point in the spanwise profile of streamwise velocity. These factors suggest a change of the most unstable mode from an outer varicose instability to an inner sinuous mode as the streak travels downstream due to the subsiding APG.

Figure 19(c) displays the results for $TI = 4.5\%$. The profile at $x = 0.2$, $T = 0$ indicates an outer mode well predicted by secondary stability analysis. The mode type remains the same at $x = 0.25$, $T = 0.05$ and $x = 0.3$, $T = 0.1$, with phase speed $c_p = 0.59 u_e$. Furthermore, the maximum disturbance amplitude lies near the maximum spanwise shear and inflection point, suggesting a sinuous mode. The predominance of outer modes for $TI = 4.5\%$ agrees with the fact that the MFD stabilises the inner mode for increasing TI . This also indicates the occurrence of bypass transition.

3.4. Remarks on a low-frequency cutoff of the free stream turbulence

The results in § 3.2 indicate that the FST with scales employed here ($\Lambda = O(10^{-2} - 10^{-1})$) effectively generate boundary-layer perturbations. However, due to these scales being smaller than those of atmospheric turbulence on real blades ($\Lambda = O(10^1)$) (IEC 2006; Bertagnolio *et al.* 2015), a cutoff scale, above which FST does not significantly influence transition, cannot be numerically established.

Low wavenumbers and, by Taylor's frozen turbulence hypothesis, low frequencies in the FST are associated with large eddies or gusts, which modify the flow by a change in AoA and Re_c (Reeh 2014; Reeh & Tropea 2015). Generally, one is typically interested in studying statistically stationary transition processes for a given flow. Unsteady effects are not substantial for $\pi f^* c / U_\infty < 0.05$ (Leishman 2016), yielding $f < 0.016 = f_{c1}$ here, where f_{c1} can be considered the first cutoff frequency. The maximum atmospheric turbulence energy occurs at $f^* = 0.01$ Hz or $f = f^* c / U_\infty = O(10^{-3})$ since typically, $c / U_\infty = O(10^{-1})$ s in wind turbines. Thus, the blade sees a steady flow regarding the most energetic eddies in the atmospheric turbulence and f_{c1} is a first frequency cutoff. Indeed, there is no significant time variation in the pressure distribution due to FST for

$TI \leq 2.4\%$, as shown in [Appendix C](#), which is the range of TI where TS waves may be relevant.

A higher frequency cutoff f_{c_2} for natural transition is estimated by noting that TS waves develop for $2\pi f^* \nu 10^6 / U_\infty^2 \geq F_L$, where $F_L = F_L(Re_c, \partial p / \partial x)$ is the lowest unstable reduced frequency (Schmid & Henningson 2001). Moreover, $F_L = F_L(TI)$, where F_L is a monotonically increasing function of TI (see [figure 10b](#)). Therefore, results for $TI = 0\%$ provide a lower bound for F_L , as sought for estimating f_{c_2} . The inequality is rewritten as

$$f \geq f_{c_2} = (2\pi)^{-1} 10^{-6} F_L Re_c. \quad (3.1)$$

The latter can be written in terms of the streamwise wavelength (λ_x) as

$$\lambda_x \leq 2\pi 10^6 c_s F_L^{-1} Re_c^{-1}, \quad (3.2)$$

where c_s is the phase speed of TS waves. Due to scale reduction, the maximum wavelength of fluctuations exciting TS waves should be retro-estimated at the leading edge (λ_{LE}). Goldstein (1983) proposed a model for scale reduction for a flat plate in which

$$\lambda_x \propto [2\pi f^* x^* / U_\infty]^{-1/2}. \quad (3.3)$$

The right-hand side of (3.3) evaluated at $x^* = c$ gives $10^3 F_L^{-1/2} Re_c^{-1/2}$, which is equivalent to the maximum factor of reduction of λ_x along the aerofoil. Dividing both sides of (3.2) by this factor yields

$$\lambda_{LE} \leq 2\pi 10^3 c_s F_L^{-1/2} Re_c^{-1/2} = \lambda_{c_2}, \quad (3.4)$$

or in terms of the cutoff wavenumber,

$$k_{c_2} = 2\pi / \lambda_{c_2} = 10^{-3} c_s^{-1} F_L^{1/2} Re_c^{1/2}. \quad (3.5)$$

There are two unknowns in (3.5). The first is c_s , which may be taken as a lower bound for the phase speed (e.g. $c_s = c_s^* / U_\infty = 0.36$). The second is F_L , a more complicated quantity to estimate as previous knowledge of the neutral curve is necessary. The naive assumption is to consider a fit for F_L extracted from the neutral curve (Schmid & Henningson 2001) for Blasius flow (Blasius 1913), which disregards flow acceleration and curvature. The expression is given by

$$F_L = 8.5775 \times 10^7 Re_x^{-1.1243}, \quad (3.6)$$

valid for $Re_x = 9 \times 10^4 - 9 \times 10^6$. For $Re_c = 1 \times 10^6$, $F_L = 15.4$ and $\lambda_{c_2} = 0.58$. The more refined method is to obtain the neutral curves of the wind turbine flow with linear stability analysis, as shown in [figure 10\(b\)](#). Due to an LSB for $TI = 0\%$, which is not present for higher TI , F_L was extracted for $TI = 0.6\%$, yielding $F_L = 17.7$ and $\lambda_{c_2} = 0.54$. These results are close to those obtained by assuming the neutral curve for Blasius flow. Interestingly, the largest integral length scale of the FST $\Lambda_{\bar{x}} = 0.211$ is lower than $\lambda_{c_2} = 0.54$, which may explain the efficiency of the FST in exciting the boundary layer. Note that the developed cutoff wavenumber estimate is only valid for TS waves and is based on the two-dimensional Goldstein model. Validation against experimental transition data is necessary to assess its validity in a complex flow under FST.

4. Conclusions

Laminar–turbulent transition on the suction surface of a section of the LM45.3p blade (20% thickness), with chord Reynolds number of 10^6 and angle of attack of 4.6° , was studied with wall-resolved large eddy simulation (LES). The blade was subject to

anisotropic free stream turbulence (FST) with turbulence intensities $TI = 0\%$, 0.6% , 1.2% , 2.4% , 4.5% and 7% . The upper bound is selected based on the experimental observation by Özçakmak *et al.* (2020). The integral length scales correspond to scaled-down values from atmospheric measurements.

For $TI = 0\%$, a laminar separation bubble (LSB) forms in the mid-chord region, and transition ensues via the breakdown of Kelvin–Helmholtz (KH) vortices. The lift-up mechanism is very robust at $Re_c = 10^6$ so that even low levels of FST (e.g. $TI = 0.6\%$) suppress the LSB due to the strong streak growth, unlike at $Re_c = 10^5$ (Fava *et al.* 2023c). Two-dimensional Tollmien–Schlichting (TS) waves play a clear role in transition for $TI = 0.6\%$. Considering $TI = 1.2\%$ and 2.4% , the flows become weakly unstable or stable to TS waves in the mean sense. The distortions generated by the streaks are essential for triggering instabilities leading to transition in these cases. The analysis of breakdown events indicates transition via inner and outer varicose modes for $TI = 1.2\%$ and 2.4% , driven by the wall-normal shear and inflectional velocity profile. However, the latter case also displays inner sinuous modes related to the spanwise shear and inflectional velocity profile preceding transition. In summary, the following conclusions can be drawn regarding $0 < TI \leq 2.4\%$:

- (i) a linear receptivity occurs, and optimal perturbation theory describes the initial streak growth and profiles well;
- (ii) transition occurs via two-dimensional TS waves for $TI = 0.6\%$, and via predominantly varicose inner and outer modes for $TI = 1.2\%$ and $TI = 2.4\%$;
- (iii) Mack’s correlation between the critical N factor and TI displays good agreement with the simulations;
- (iv) the critical disturbance kinetic energy is proportional to $TI^{-1.80 \pm 0.11}$.

The $TI = 2.4\%$ case represents an intermediate state towards bypass transition. For $TI \geq 2.4\%$, the FST induces high-frequency boundary layer perturbations, although nonlinear receptivity of the leading streaks is not observed. Particularly for $TI \geq 4.5\%$, the streaks are generated with a high amplitude near the leading edge and grow little due to lift-up. The subsequent conclusions can be drawn for these cases:

- (i) the scaling of the leading streamwise velocity perturbations with TI is sub-linear, although high-frequency disturbances are possibly nonlinearly generated in the boundary layer;
- (ii) bypass transition occurs with the dominance of breakdowns via outer sinuous modes, driven by the spanwise shear and inflectional velocity profile;
- (iii) the turbulent breakdown is highly non-uniform in the spanwise direction;
- (iv) the critical disturbance kinetic energy is proportional to $TI^{-0.90 \pm 0.16}$, an exponent half of that of the modal regime.

The inception of bypass transition between $TI = 2.4\%$ and 4.5% agrees with $TI = 3\%$ found by Brandt *et al.* (2004) for the Blasius boundary layer and Hosseinverdi & Fasel (2019) for a flat plate with flow separation. Finally, an estimate for a low-frequency/low-wavenumber cutoff for the turbulence spectrum affecting transition via TS waves is proposed. This allows for obtaining an effective TI from atmospheric turbulence measurements, compatible with wind tunnel data and Mack’s correlation.

Funding. This work was possible with funding from StandUp for Wind, and HPC resources provided by the North-German Supercomputing Alliance (HLRN) and the Swedish National Infrastructure for Computing (SNIC).

Declaration of interests. The authors report no conflict of interest.

Author contributions. B.A.L. ran the simulations. T.C.L.F. developed post-processing tools and carried out the analyses of the results with B.A.L. T.C.L.F. and B.A.L. wrote the paper with feedback from A.P.S., M.B., D.S.H. and A.H.

Data availability statement. Data are available upon request.

Appendix A. Calculation of coefficients and errors of the N factor correlations

The calculation of the regression coefficients was performed according to Neter *et al.* (1996) as

$$(a, b)^T = (\mathbf{X}^T \mathbf{X})^{-1} \mathbf{X}^T \mathbf{N}, \quad (\text{A1})$$

where \mathbf{N} is the vector of critical N factors from the LES and

$$\mathbf{X} = \begin{pmatrix} 1 & -\ln(TI_1/100) \\ \vdots & \vdots \\ 1 & -\ln(TI_n/100) \end{pmatrix}. \quad (\text{A2})$$

The errors of the coefficients a and b were estimated as

$$(\sigma_a, \sigma_b)^T = \text{diag} \left[\sqrt{\hat{\sigma}^2 (\mathbf{X}^T \mathbf{X})^{-1}} \right], \quad (\text{A3})$$

$$\hat{\sigma}^2 = \frac{\sum_{i=1}^n (N_i - \tilde{N}_i)^2}{n - 2}, \quad (\text{A4})$$

where N and \tilde{N} are the critical N factors from the LES and correlations, respectively. The procedure is applied to the low- TI range, which contains the points $TI = 0.6\%$, 1.2% and 2.4% , yielding the coefficients $a = 2.63$ and $b = 1.8$ with corresponding errors $\sigma_a = 0.51$ and $\sigma_b = 0.11$. For the high- TI range, containing the points $TI = 2.4\%$, 4.5% and 7% , the coefficients are $a = 1.81$ and $b = 0.9$ with errors $\sigma_a = 0.50$ and $\sigma_b = 0.16$, respectively.

Appendix B. Operators for secondary stability analysis

The secondary stability analysis of the streaks was carried out with the two-dimensional eigenvalue problem over the cross-sectional planes (Siconolfi *et al.* 2015). The method was obtained by introducing the ansatz $\mathbf{q}' = \hat{\mathbf{q}}(y, z) \exp(i\alpha x - i\omega t)$ in the linearised Navier–Stokes equations (equations for the momentum in x , y , z , and continuity equation) with non-local terms dropped, where $\mathbf{q}'(x, y, z, t) = [u' v' w' p']^T$ is the vector of perturbations of pressure (p'), and streamwise (u'), wall-normal (v') and spanwise (w') velocities. Here, $\alpha = \alpha_r + i\alpha_i$, where α_r is the streamwise wavenumber and α_i is the spatial growth rate. Additionally, $\omega = 2\pi f \in \mathbb{R}$ is the angular frequency, an input in the spatial framework employed here. The resulting generalised eigenvalue problem, solved for α , $\hat{\mathbf{q}}$ and $\alpha\hat{\mathbf{q}}$, is given by

$$\begin{pmatrix} \mathcal{A} & \mathbf{0} \\ \mathbf{0} & \mathbf{I} \end{pmatrix} \begin{pmatrix} \hat{\mathbf{q}} \\ \alpha\hat{\mathbf{q}} \end{pmatrix} = \alpha \begin{pmatrix} \mathcal{B} & \mathcal{C} \\ \mathbf{I} & \mathbf{0} \end{pmatrix} \begin{pmatrix} \hat{\mathbf{q}} \\ \alpha\hat{\mathbf{q}} \end{pmatrix}, \quad (\text{B1})$$

$$\mathcal{A} = \begin{pmatrix} \mathcal{A}_{11} & \overline{U}_y & \overline{U}_z & 0 \\ 0 & \mathcal{A}_{22} & \overline{V}_z & \mathcal{D}_y \\ 0 & \overline{W}_y & \mathcal{A}_{33} & \mathcal{D}_z \\ 0 & \mathcal{D}_y & \mathcal{D}_z & 0 \end{pmatrix}, \quad (\text{B2})$$

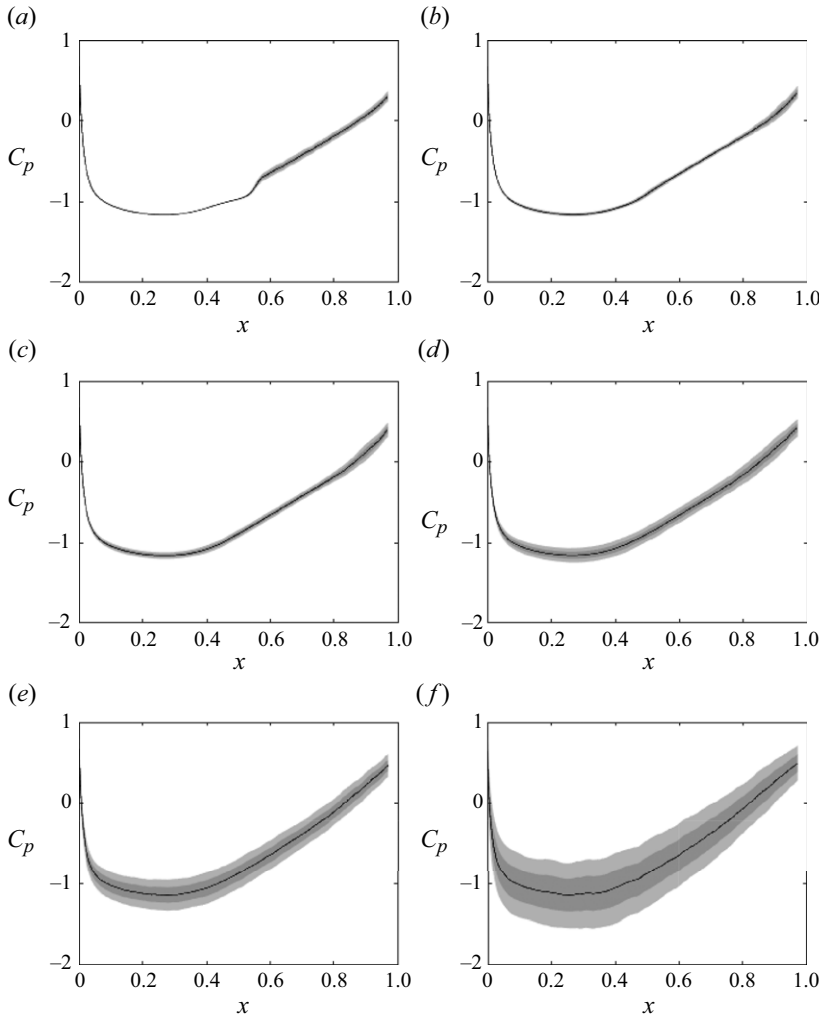


Figure 20. Mean pressure distribution on the suction side (black line) for (a) $Tl = 0\%$, (b) 0.6% , (c) 1.2% , (d) 2.4% , (e) 4.5% and (f) 7% . The shaded regions indicate one and two standard deviations around the mean.

$$\mathcal{B} = - \begin{pmatrix} i\overline{U} & 0 & 0 & i \\ 0 & i\overline{U} & 0 & 0 \\ 0 & 0 & i\overline{U} & 0 \\ i & 0 & 0 & 0 \end{pmatrix}, \quad \mathcal{C} = -\frac{1}{Re_c} \begin{pmatrix} 1 & 0 & 0 & 0 \\ 0 & 1 & 0 & 0 \\ 0 & 0 & 1 & 0 \\ 0 & 0 & 0 & 0 \end{pmatrix}, \quad (\text{B3})$$

$$\mathcal{A}_{11} = \overline{V}\mathcal{D}_y + \overline{W}\mathcal{D}_z - \frac{1}{Re_c} (\mathcal{D}_{yy} + \mathcal{D}_{zz}) - i\omega, \quad (\text{B4})$$

$$\mathcal{A}_{22} = \overline{V}\mathcal{D}_y + \overline{W}\mathcal{D}_z - \frac{1}{Re_c} (\mathcal{D}_{yy} + \mathcal{D}_{zz}) + \overline{V}_y - i\omega, \quad (\text{B5})$$

$$\mathcal{A}_{33} = \overline{V}\mathcal{D}_y + \overline{W}\mathcal{D}_z - \frac{1}{Re_c} (\mathcal{D}_{yy} + \mathcal{D}_{zz}) + \overline{W}_z - i\omega, \quad (\text{B6})$$

where \mathcal{D}_y and \mathcal{D}_z are the derivatives in the y and z directions, obtained with a fourth-order finite-difference approximation; \mathbf{I} and $\mathbf{0}$ are the identity and null matrices.

The vector of base-flow variables is given by $\bar{\mathbf{q}} = [\bar{U} \ \bar{V} \ \bar{W} \ \bar{P}]^T$, where \bar{P} is the pressure, and \bar{U} , \bar{V} and \bar{W} are the streamwise, wall-normal and spanwise velocities. Subscripts y and z indicate derivatives in the y and z directions, respectively. Here, $i = \sqrt{-1}$ is the imaginary unity; Re_c is the Reynolds number. The boundary conditions are $u' = v' = w' = 0$ at $y = 0$ (wall), $y \rightarrow \infty$ (free stream). Furthermore, a periodic boundary condition is imposed in the spanwise direction, such that $\mathbf{q}'(x, y, z, t) = \mathbf{q}'(x, y, z + L_z, t)$, where L_z is the spanwise width. The grid comprises 150 and 96 points in the z and y directions, respectively.

Appendix C. Non-stationarity of the pressure distributions due to the FST

Figure 20 shows the statistics of the pressure distribution on the aerofoil suction side. The mean distribution is shown with a black line, whereas the regions with one and two standard deviations around the mean are shown with shades of grey. There is little non-stationarity for $TI \leq 2.4\%$. However, the $TI = 7\%$ case presents a high degree of non-stationarity, with significant oscillations in the angle of attack and Reynolds number. However, this is not enough to cause instantaneous flow separation.

REFERENCES

- AMANDOLÈSE, X. & SZÉCHÉNYI, E. 2004 Experimental study of the effect of turbulence on a section model blade oscillating in stall. *Wind Energy* **7** (4), 267–282.
- ANDERSSON, P., BERGGREN, M. & HENNINGSON, D.S. 1999 Optimal disturbances and bypass transition in boundary layers. *Phys. Fluids* **11** (1), 134–150.
- ANDERSSON, P., BRANDT, L., BOTTARO, A. & HENNINGSON, D.S. 2001 On the breakdown of boundary layer streaks. *J. Fluid Mech.* **428**, 29–60.
- ARNAL, D. & CASALIS, G. 2000 Laminar-turbulent transition prediction in three-dimensional flows. *Prog. Aerosp. Sci.* **36** (2), 173–191.
- ARNAL, D. & JUILLEN, J.C. 1978 Contribution expérimentale à l'étude de la receptivité d'une couche limite laminaire à la turbulence de l'écoulement général. 1/5018. ONERA.
- ASADA, K. & KAWAI, S. 2018 Large-eddy simulation of airfoil flow near stall condition at Reynolds number 2.1×10^6 . *Phys. Fluids* **30** (8), 1139–1145.
- ASAI, M., MINAGAWA, M. & NISHIOKA, M. 2002 The instability and breakdown of a near-wall low-speed streak. *J. Fluid Mech.* **455**, 289–314.
- BALAMURUGAN, G. & MANDAL, A.C. 2017 Experiments on localized secondary instability in bypass boundary layer transition. *J. Fluid Mech.* **817**, 217–263.
- BERLIN, S., WIEGEL, M. & HENNINGSON, D.S. 1999 Numerical and experimental investigations of oblique boundary layer transition. *J. Fluid Mech.* **393**, 23–57.
- BERTAGNOLIO, F., MADSEN, H.A., BAK, CH, TROLDORG, N. & FISCHER, A. 2015 Aerodynamic noise characterization of a full-scale wind turbine through high-frequency surface pressure measurements. *Intl J. Aeroacoust.* **14** (5–6), 729–766.
- BERTOLOTI, F.P. 1997 Response of the Blasius boundary layer to free-stream vorticity. *Phys. Fluids* **9** (8), 2286–2299.
- BLANCO, D.C.P., HANIFI, A., HENNINGSON, D.S. & CAVALIERI, A.V.G. 2024 Linear and nonlinear receptivity mechanisms in boundary layers subject to free-stream turbulence. *J. Fluid Mech.* **979**, A31.
- BLASIUS, H. 1913 Das Ähnlichkeitsgesetz bei reibungsvorgängen. *Mitteilungen über Forschungsarbeiten auf dem Gebiete des Ingenieurwesens insbesondere aus den Laboratorien der technischen Hochschulen herausgegeben vom Verein deutscher Ingenieure* **131**, 1–39.
- BOIKO, A.V., GREK, G.R., DOVGAL, A.V. & KOZLOV, V.V. 2002 *The Origin of Turbulence in Near-Wall Flows*. Springer Berlin, Heidelberg.
- BOIKO, A.V., WESTIN, K.J.A., KLINGMANN, B.G.B., KOZLOV, V.V. & ALFREDSSON, P.H. 1994 Experiments in a boundary layer subjected to free stream turbulence. Part 2. The role of TS-waves in the transition process. *J. Fluid Mech.* **281**, 219–245.
- BOSE, R. & DURBIN, P.A. 2016 Transition to turbulence by interaction of free-stream and discrete mode perturbations. *Phys. Fluids* **28** (11), 1–19.
- BRANDT, L. & DE LANGE, H.C. 2008 Streak interactions and breakdown in boundary layer flows. *Phys. Fluids* **20** (2), 1–16.

- BRANDT, L., SCHLATTER, P. & HENNINGSON, D.S. 2004 Transition in boundary layers subject to free-stream turbulence. *J. Fluid Mech.* **517**, 167–198.
- BREUER, M. 1998 Large-eddy simulation of the sub-critical flow past a circular cylinder: numerical and modeling aspects. *Int. J. Numer. Meth. Fl.* **28** (9), 1281–1302.
- BREUER, M. 2000 A challenging test case for large-eddy simulation: high Reynolds number circular cylinder flow. *Intl J. Heat Fluid Flow* **21** (5), 648–654.
- BREUER, M. 2018 Effect of inflow turbulence on an airfoil flow with laminar separation bubble: an LES study. *Flow Turbul. Combust.* **101** (2), 433–456.
- BREUER, M. & SCHMIDT, S. 2019 Effect of inflow turbulence on LES of an airfoil flow with laminar separation bubble. In *ERCOTAC Series, Direct and Large-Eddy Simulation XI, 11th International ERCOTAC Workshop on Direct and Large-Eddy Simulation: DLES-11, Pisa, Italy, May 29-31, 2017*, pp. 351–357. Springer Nature Switzerland AG.
- BRINKERHOFF, J.R. & YARAS, M.I. 2015 Numerical investigation of transition in a boundary layer subjected to favourable and adverse streamwise pressure gradients and elevated free stream turbulence. *J. Fluid Mech.* **781**, 52–86.
- BUTLER, K.M. & FARRELL, B.F. 1992 Three-dimensional optimal perturbations in viscous shear flow. *Phys. Fluids A* **4** (8), 1637–1650.
- CHERUBINI, S., ROBINET, J.-CH & DE PALMA, P. 2010 The effects of non-normality and nonlinearity of the Navier–Stokes operator on the dynamics of a large laminar separation bubble. *Phys. Fluids* **22** (1), 014102.
- COSSU, C. & BRANDT, L. 2004 On Tollmien–Schlichting-like waves in streaky boundary layers. *Eur. J. Mech. B/Fluids* **23** (6), 815–833.
- CRAIK, A.D.D. 1971 Non-linear resonant instability in boundary layers. *J. Fluid Mech.* **50** (2), 393–413.
- DE NAYER, G., SCHMIDT, S., WOOD, J.N. & BREUER, M. 2018 Enhanced injection method for synthetically generated turbulence within the flow domain of eddy-resolving simulations. *Comput. Maths Applics.* **75** (7), 2338–2355.
- DOLLINGER, CH, BALARESQUE, N., GAUDERN, N., GLEICHAUF, D., SORG, M. & FISCHER, A. 2019 IR thermographic flow visualization for the quantification of boundary layer flow disturbances due to the leading edge condition. *Renew. Energy* **138**, 709–721.
- DØSSING, M. 2008 *High frequency microphone measurements for transition detection on airfoils*. Risø National Laboratory, Technical University of Denmark, pp. 1–23.
- DOTTO, A., BARSI, D., LENGANI, D., SIMONI, D. & SATTA, F. 2022 Effect of free-stream turbulence properties on different transition routes for a zero-pressure gradient boundary layer. *Phys. Fluids* **34** (5), 1–16.
- DURBIN, P.A. 2017 Perspectives on the phenomenology and modeling of boundary layer transition. *Flow Turbul. Combust.* **99** (1), 1–23.
- FASEL, H.F. 2002 Numerical investigation of the interaction of the Klebanoff-mode with a Tollmien–Schlichting wave. *J. Fluid Mech.* **450**, 1–33.
- FAÚNDEZ ALARCÓN, J.M., MORRA, P., HANIFI, A. & HENNINGSON, D.S. 2022 Disturbance growth on a NACA0008 wing subjected to free stream turbulence. *J. Fluid Mech.* **944**, A44.
- FAVA, T.C.L., HENNINGSON, D.S. & HANIFI, A. 2023a Influence of free-stream turbulence on the boundary layer stability of a wind turbine airfoil and near wake: PSE operators. *HAL* **2505** (1), hal-04075160.
- FAVA, T.C.L., HENNINGSON, D.S. & HANIFI, A. 2024a Boundary layer stability on a rotating wind turbine blade section. *Phys. Fluids* **36** (9), 094128.
- FAVA, T.C.L., LOBO, B.A., NOGUEIRA, P.A.S., SCHAFFARCZYK, A.P., BREUER, M., HENNINGSON, D.S. & HANIFI, A. 2023b Influence of free-stream turbulence on the boundary layer stability of a wind turbine airfoil and near wake. *J. Phys.: Conf. Ser.* **2505** (1), 012002.
- FAVA, T.C.L., LOBO, B.A., NOGUEIRA, P.A.S., SCHAFFARCZYK, A.P., BREUER, M., HENNINGSON, D.S. & HANIFI, A. 2023c Numerical study of the hydrodynamic stability of a wind-turbine airfoil with a laminar separation bubble under free-stream turbulence. *Phys. Fluids* **35** (8), 1–26.
- FAVA, T.C.L., MASSARO, D., SCHLATTER, P., HENNINGSON, D.S. & HANIFI, A. 2024b Transition to turbulence on a rotating wind turbine blade at $Re_c = 3 \times 10^5$. *J. Fluid Mech* **999**, A54.
- FRANSSON, J.H.M., BRANDT, L., TALAMELLI, A. & COSSU, C. 2005 Experimental study of the stabilization of Tollmien–Schlichting waves by finite amplitude streaks. *Phys. Fluids* **17** (5), 054110.
- GERMANO, M., PIOMELLI, U., MOIN, P. & CABOT, W.H. 1991 A dynamic subgrid-scale eddy viscosity model. *Phys. Fluids A: Fluid Dyn.* **3** (7), 1760–1765.
- GOLDSTEIN, M.E. 1983 The evolution of Tollmien–Schlichting waves near a leading edge. *J. Fluid Mech.* **127**, 59–81.
- HACK, M.J.P. & ZAKI, T.A. 2014 Streak instabilities in boundary layers beneath free-stream turbulence. *J. Fluid Mech* **741**, 280–315.

- HAND, M.M., KELLEY, N.D. & BALAS, M.J. 2003 Identification of wind turbine response to turbulent inflow structures. In *4th ASME/JSME Joint Fluids Engineering Conference*, pp. 2557–2566. The American Society of Mechanical Engineers.
- HERBERT, T. 1997 Parabolized stability equations. *Annu. Rev. Fluid Mech.* **29** (1), 245–283.
- HØJSTRUP, J. 1999 Spectral coherence in wind turbine wakes. *J. Wind Engng Ind. Aerodyn.* **80** (1–2), 137–146.
- HOSSEINVERDI, S. & FASEL, H.F. 2019 Numerical investigation of laminar-turbulent transition in laminar separation bubbles: the effect of free-stream turbulence. *J. Fluid Mech.* **858**, 714–759.
- HUNT, J.C.R. & CARRUTHERS, D.J. 1990 Rapid distortion theory and the ‘problems’ of turbulence. *J. Fluid Mech.* **212** (1), 497–532.
- IEC 2006 *Wind Turbines – Part 1: Design Requirements*. IEC 61400-1. IEC.
- VAN INGEN, J. 2008 The e^N method for transition prediction. Historical review of work at TU Delft. In *38th Fluid Dynamics Conference and Exhibit*, pp. 3830. American Institute of Aeronautics and Astronautics.
- VAN INGEN, J.L. 1956 A suggested semi-empirical method for the calculation of the boundary layer transition region. Tech. Rep. VTH-71. Delft University.
- ISTVAN, M.S. & YARUSEVYCH, S. 2018 Effects of free-stream turbulence intensity on transition in a laminar separation bubble formed over an airfoil. *Exp. Fluids* **59** (3), 52.
- JACOBS, R.G. & DURBIN, P.A. 1998 Shear sheltering and the continuous spectrum of the Orr–Sommerfeld equation. *Phys. Fluids* **10** (8), 2006–2011.
- JAROSLAWSKI, T., FORTE, M., VERMEERSCH, O., MOSCHETTA, J.-M. & GOWREE, E.R. 2023 Disturbance growth in a laminar separation bubble subjected to free-stream turbulence. *J. Fluid Mech.* **956**, A33.
- JEROMIN, A., SCHAFFARCZYK, A.P., PUCZYLOWSKI, J., PEINKE, J. & HÖLLING, M. 2014 Highly resolved measurements of atmospheric turbulence with the new 2D-atmospheric laser cantilever anemometer. *J. Phys.: Conf. Ser.* **555**, 012054.
- JONKMAN, B.J. 2009 TurbSim user’s guide: version 1.50, NREL/TP-500-46198. National Renewable Energy Laboratory.
- KAIMAL, J.C. 1973 Turbulence spectra, length scales and structure parameters in the stable surface layer. *Boundary-Layer Meteorol.* **4** (1–4), 289–309.
- KEMPF, A.M., WYSOCKI, S. & PETTIT, M. 2012 An efficient, parallel low-storage implementation of Klein’s turbulence generator for LES and DNS. *Comput. Fluids* **60**, 58–60.
- KENDALL, J.M. 1990 Boundary layer receptivity to freestream turbulence. In *21st Fluid Dynamics, Plasma Dynamics and Lasers Conference*, pp. 1504. American Institute of Aeronautics and Astronautics.
- KLEBANOFF, P.S. 1971 Effect of free-stream turbulence on a laminar boundary layer. *Bull. Am. Phys. Soc.* **16**, 1323.
- KLEIN, M., SADIKI, A. & JANICKA, J. 2003 A digital filter based generation of inflow data for spatially developing direct numerical or large eddy simulations. *J. Comput. Phys.* **186** (2), 652–665.
- LANDAHL, M.T. 1975 Wave breakdown and turbulence. *SIAM J. Appl. Maths* **28** (4), 735–756.
- LANDAHL, M.T. 1980 A note on an algebraic instability of inviscid parallel shear flows. *J. Fluid Mech.* **98** (2), 243–251.
- LEISHMAN, J.G. 2016 *Principles of Helicopter Aerodynamics*. 2nd edn. Cambridge University Press.
- LILLY, D.K. 1992 A proposed modification of the Germano subgrid-scale closure method. *Phys. Fluids A: Fluid Dyn.* **4** (3), 633–635.
- LIU, Y., ZAKI, T.A. & DURBIN, P.A. 2008 Floquet analysis of secondary instability of boundary layers distorted by Klebanoff streaks and Tollmien–Schlichting waves. *Phys. Fluids* **20** (12), 124102.
- LOBO, B.A. 2023 Investigation into boundary layer transition on a wind turbine airfoil using wall-resolved large-eddy simulations and modeled inflow turbulence. *PhD thesis*, Helmut-Schmidt-Universität / Universität der Bundeswehr Hamburg, Hamburg, Germany.
- LOBO, B.A., BOORSMA, K. & SCHAFFARCZYK, A.P. 2018 Investigation into boundary layer transition on the MEXICO blade. *J. Phys.: Conf. Ser.* **1037**, 052020.
- LOBO, B.A., ÖZÇAKMAK, O.S., MADSEN, H.A., SCHAFFARCZYK, A.P., BREUER, M. & SØRENSEN, N.N. 2023 On the laminar–turbulent transition mechanism on megawatt wind turbine blades operating in atmospheric flow. *Wind Energy Sci.* **8** (3), 303–326.
- LOBO, B.A., SCHAFFARCZYK, A.P. & BREUER, M. 2022 Investigation into boundary layer transition using wall-resolved large-eddy simulations and modeled inflow turbulence. *Wind Energy Sci.* **7** (3), 967–990.
- LUCHINI, P. 2000 Reynolds-number-independent instability of the boundary layer over a flat surface: optimal perturbations. *J. Fluid Mech.* **404**, 289–309.
- LUMLEY, J.L. 1970 *Stochastic Tools in Turbulence*. 1st edn. Academic Press.
- LUND, T.S., WU, X. & SQUIRES, K.D. 1998 Generation of turbulent inflow data for spatially-developing boundary layer simulations. *J. Comput. Phys.* **140** (2), 233–258.

- MACK, L.M. 1977 Transition and laminar instability, NASA-CR-153203. Jet Propulsion Laboratory, California Institute of Technology.
- MADSEN, H.A., BAK, C., PAULSEN, U.S., GAUNAA, M., FUGLSANG, P., ROMBLAD, J., OLESEN, N.A., ENEVOLDSEN, P., LAURSEN, J. & JENSEN, L. 2010 The DAN-AERO MW experiments: final report. Risø-R-1726(EN). DTU Wind Energy.
- MADSEN, H.A., ÖZÇAKMAK, S., BAK, C., TROLDBORG, N., SØRENSEN, N.N. & SØRENSEN, J.N. 2019 Transition characteristics measured on a 2 MW 80m diameter wind turbine rotor in comparison with transition data from wind tunnel measurements. In *AIAA Scitech 2019 Forum*, pp. 1–15. American Institute of Aeronautics and Astronautics.
- MALDONADO, V., CASTILLO, L., THORMANN, A. & MENEVEAU, C. 2015 The role of free stream turbulence with large integral scale on the aerodynamic performance of an experimental low Reynolds number S809 wind turbine blade. *J. Wind Engng Ind. Aerodyn.* **142**, 246–257.
- MANDAL, A.C., VENKATAKRISHNAN, L. & DEY, J. 2010 A study on boundary-layer transition induced by free-stream turbulence. *J. Fluid Mech.* **660**, 114–146.
- MANS, J., KADIJK, E.C., DE LANGE, H.C. & VAN STEENHOVEN, A.A. 2005 Breakdown in a boundary layer exposed to free-stream turbulence. *Exp. Fluids* **39** (6), 1071–1083.
- MANS, J., DE LANGE, H.C. & VAN STEENHOVEN, A.A. 2007 Sinuous breakdown in a flat plate boundary layer exposed to free-stream turbulence. *Phys. Fluids* **19** (8), 088101.
- MARQUILLIE, M., EHRENSTEIN, U. & LAVAL, J.-P. 2011 Instability of streaks in wall turbulence with adverse pressure gradient. *J. Fluid Mech.* **681**, 205–240.
- MARXEN, O., LANG, M., RIST, U. & WAGNER, S. 2003 A combined experimental/numerical study of unsteady phenomena in a laminar separation bubble. *Flow Turbul. Combust.* **71** (1–4), 133–146.
- MARXEN, O. & RIST, U. 2010 Mean flow deformation in a laminar separation bubble: separation and stability characteristics. *J. Fluid Mech.* **660**, 37–54.
- MORKOVIN, M.V. 1969 On the many faces of transition. In *Viscous Drag Reduction* (ed. C.S. WELLS), pp. 1–31. Springer US.
- NAGARAJAN, S., LELE, S.K. & FERZIGER, J.H. 2007 Leading-edge effects in bypass transition. *J. Fluid Mech.* **572**, 471–504.
- NETER, J., KUTNER, M.H., NACHTSHEIM, C.J. & WASSERMAN, W. 1996 *Applied Linear Statistical Models*. Irwin.
- NODA, M. & FLAY, R.G.J. 1999 A simulation model for wind turbine blade fatigue loads. *J. Wind Engng Ind. Aerodyn.* **83** (1–3), 527–540.
- OEHME, F., GLEICHAUF, D., SUHR, J., BALARESQUE, N., SORG, M. & FISCHER, A. 2022 Thermographic detection of turbulent flow separation on rotor blades of wind turbines in operation. *J. Wind Engng Ind. Aerodyn.* **226**, 105025.
- O’NEILL, P., NICOLAIDES, D., HONNERY, D. & SORIA, J. 2004 Autocorrelation functions and the determination of integral length with reference to experimental and numerical data. In *15th Australasian Fluid Mechanics Conference*, vol. 1, pp. 1–4. University of Sydney.
- ÖZÇAKMAK, O.S., MADSEN, H.A., SØRENSEN, N.N. & SØRENSEN, J.N. 2020 Laminar-turbulent transition characteristics of a 3-D wind turbine rotor blade based on experiments and computations. *Wind Energy Sci.* **5** (4), 1487–1505.
- PERRY, A.E., LIM, T.T. & TEH, E.W. 1981 A visual study of turbulent spots. *J. Fluid Mech.* **104**, 387–405.
- PIOMELLI, U. & CHASNOV, J.R. 1996 Large-eddy simulations: theory and applications. In *Turbulence and Transition Modeling*, (ed. M. HALLBÄCK, D.S. HENNINGSON, A.V. JOHANSSON & P.H. ALFREDSON), pp. 269–331. Kluwer.
- REED, H.L., SARIC, W.S. & ARNAL, D. 1996 Linear stability theory applied to boundary layers. *Annu. Rev. Fluid Mech.* **28** (1), 389–428.
- REEH, A.D. 2014 Natural laminar flow airfoil behavior in cruise flight through atmospheric turbulence. *PhD thesis*, Technische Universität Darmstadt, Darmstadt.
- REEH, A.D. & TROPEA, C. 2015 Behaviour of a natural laminar flow aerofoil in flight through atmospheric turbulence. *J. Fluid Mech.* **767**, 394–429.
- REICHSTEIN, T., SCHAFFARCZYK, A.P., DOLLINGER, CH, BALARESQUE, N., SCHÜLEIN, E., JAUCH, C. & FISCHER, A. 2019 Investigation of laminar-turbulent transition on a rotating wind-turbine blade of multi-megawatt class with thermography and microphone array. *Energies* **12** (11), 2102.
- RESHOTKO, E. 1976 Boundary-layer stability and transition. *Annu. Rev. Fluid Mech.* **8** (1), 311–349.
- ROMBLAD, J., GREINER, M., GUISSART, A. & WÜRZ, W. 2022 Characterization of low levels of turbulence generated by grids in the settling chamber of a laminar wind tunnel. *Exp. Fluids* **63** (4), 65.
- RUBAN, A.I. 1984 On the generation of Tollmien–Schlichting waves by sound. *Fluid Dyn.* **19** (5), 709–717.

- SARIC, W.S., REED, H.L. & KERSCHEN, E.J. 2002 Boundary-layer receptivity to freestream disturbances. *Annu. Rev. Fluid Mech.* **34** (1), 291–319.
- SAYADI, T. & MOIN, PARVIZ 2011 Predicting natural transition using large eddy simulation. In *Annual Research Briefs 2011*, pp. 97–108. Center for Turbulence Research.
- SCHAFFARCZYK, A.P., SCHWAB, D. & BREUER, M. 2017 Experimental detection of laminar–turbulent transition on a rotating wind turbine blade in the free atmosphere. *Wind Energy* **20** (2), 211–220.
- SCHLATTER, P., DEUSEBIO, E., DE LANGE, R. & BRANDT, L. 2010 Numerical study of the stabilisation of boundary-layer disturbances by finite amplitude streaks. *Intl J. Flow Control* **2** (4), 259–288.
- SCHMID, P.J. 2007 Nonmodal stability theory. *Annu. Rev. Fluid Mech.* **39** (1), 129–162.
- SCHMID, P.J. & HENNINGSON, D.S. 2001 *Stability and Transition in Shear Flows*. Springer.
- SCHMIDT, O.T. & COLONIUS, T. 2020 Guide to spectral proper orthogonal decomposition. *AIAA J.* **58** (3), 1023–1033.
- SCHMIDT, O.T. & TOWNE, A. 2019 An efficient streaming algorithm for spectral proper orthogonal decomposition. *Comput. Phys. Commun.* **237**, 98–109.
- SCHMIDT, S. & BREUER, M. 2017 Source term based synthetic turbulence inflow generator for eddy–resolving predictions of an airfoil flow including a laminar separation bubble. *Comput. Fluids* **146**, 1–22.
- SCHRADER, L.-U., BRANDT, L. & HENNINGSON, D.S. 2009 Receptivity mechanisms in three-dimensional boundary-layer flows. *J. Fluid Mech.* **618**, 209–241.
- SCHRADER, L.-U., BRANDT, L., MAVRIPLIS, C. & HENNINGSON, D.S. 2010 Receptivity to free-stream vorticity of flow past a flat plate with elliptic leading edge. *J. Fluid Mech.* **653**, 245–271.
- SICONOLFI, L., CAMARRI, S. & FRANSSON, J.H.M. 2015 Stability analysis of boundary layers controlled by miniature vortex generators. *J. Fluid Mech.* **784**, 596–618.
- SICOT, C., DEVINANT, P., LOYER, S. & HUREAU, J. 2008 Rotational and turbulence effects on a wind turbine blade. Investigation of the. *J. Wind Engng Ind. Aerodyn.* **96** (8–9), 1320–1331.
- SMAGORINSKY, J. 1963 General circulation experiments with the primitive equations. *Mon. Weather Rev.* **91** (3), 99–164.
- SMITH, A.M.O. & GAMBERONI, N. 1956 Transition, pressure gradient, and stability theory, pp. 1–59. Douglas Aircraft Co, El Segundo.
- SQUIRE, H.B. 1933 On the stability for three-dimensional disturbances of viscous fluid flow between parallel walls. *Proc. R. Soc. Lond. A*, Containing Papers of a Mathematical and Physical Character **142** (847), 621–628.
- SWEARINGEN, J.D. & BLACKWELDER, R.F. 1987 The growth and breakdown of streamwise vortices in the presence of a wall. *J. Fluid Mech.* **182**, 255–290.
- THOMSEN, K. & SØRENSEN, P. 1999 Fatigue loads for wind turbines operating in wakes. *J. Wind Eng. Ind. Aerodyn.* **80** (1–2), 121–136.
- TOWNE, A., SCHMIDT, O.T. & COLONIUS, T. 2018 Spectral proper orthogonal decomposition and its relationship to dynamic mode decomposition and resolvent analysis. *J. Fluid Mech.* **847**, 821–867.
- TROLDORF, N., BAK, C., MADSEN, H.A. & SKRZYPINSKI, W.R. 2013 DANAERO MW: final report, pp. 1–143. DTU Wind Energy.
- VAUGHAN, N.J. & ZAKI, T.A. 2011 Stability of zero-pressure-gradient boundary layer distorted by unsteady Klebanoff streaks. *J. Fluid Mech.* **681**, 116–153.
- VEERASAMY, D., ATKIN, C.J. & PONNUSAMI, S.A. 2021 Aerofoil wake-induced transition characteristics on a flat-plate boundary layer. *J. Fluid Mech.* **920**, A29.
- WYNGAARD, J.C. 1992 Atmospheric turbulence. *Annu. Rev. Fluid Mech.* **24** (1), 205–234.
- ZAKI, T.A. & DURBIN, P.A. 2005 Mode interaction and the bypass route to transition. *J. Fluid Mech.* **531**, 85–111.
- ZHAO, Y. & SANDBERG, R.D. 2020 Bypass transition in boundary layers subject to strong pressure gradient and curvature effects. *J. Fluid Mech.* **888**, A4.